Contrib Mineral Petrol (2004) 147: 484–504
DOI 10.1007/s00410-004-0569-z

ORIGINAL PAPER

José F. Molina · Stefano Poli · Håkon Austrheim
Johannes Glodny · Anatolij Rusin

Eclogite-facies vein systems in the Marun-Keu complex (Polar Urals, Russia): textural, chemical and thermal constraints for patterns of fluid flow in the lower crust

Received: 16 June 2003 / Accepted: 12 February 2004 / Published online: 23 March 2004

Abstract Metasomatic amphibole-eclogite sequences grew in selvages of quartz veins from the Marun-Keu complex (Polar Urals, Russia) during high-pressure metamorphism. Relicts of a pre-metasomatic eclogite-facies assemblage are present in the wallrock layers as irregular patches. Wallrock interstitial quartz trails lying at a high angle to reaction fronts provide evidence for grain-scale pore channelisation which may be produced by intergranular-fluid compositional gradients parallel to the quartz trails. Disequilibrium at vein-wallrock scale is inferred from wallrock mineral heterogeneity and from variable initial Sr isotope ratios in mineral separates. Mass-balance calculations between relicts and wallrock assemblages reveal chemical imbalances caused by open system-behaviour with two way mass-transfer. The vein-wallrock system registers a prograde history from 408–434 °C (relicts) to 526–668 °C (vein precipitates). Vein and metasomatic assemblages formed during a single fluid-rock interaction process, implying high heating rates (≥100 °C/Ma), which could result from heat advection by large-scale fluid circulation.

Editorial responsibility: W. Schreyer

J. F. Molina (✉)
Departamento de Mineralogía y Petrología, Facultad de Ciencias, Universidad de Granada, Fuentenueva s/n, 18002 Granada, Spain
E-mail: jfmolina@ugr.es
Fax: +34-958-243368

J. F. Molina · S. Poli
Dipartimento Scienze della Terra, Università degli Studi di Milano, Via Botticelli 23, 20133 Milan, Italy

H. Austrheim
PGP and Department of Geosciences, Postboks 1047, Blindern, 0316 Oslo, Norway

J. Glodny
GeoForschungsZentrum Potsdam, Telegrafenberg C2, 14473 Potsdam, Germany

A. Rusin
Institute of Geology and Geochemistry, Pochtovy per. 7, Ekaterinburg, Russia

Metamorphic fluids in high-pressure regimes

Fluid release from subducting crust transfers large amounts of volatiles and incompatible elements to the overlying mantle wedge. High-pressure experiments and calculated phase relations in basaltic systems suggest that aqueous solutions prevail in high-pressure regimes (Pawley and Holloway 1993; Yaxley and Green 1994; Schmidt and Poli 1998, 2003; Molina and Poli 2000; Kerrick and Connolly 2001; Poli and Schmidt 2002). Increasing dissolution of silicates in aqueous fluids with increasing pressure and temperature (Newton and Manning 2000) is responsible for metasomatic processes in a variety of geodynamic systems leading, as an ultimate consequence, to the variably enriched mantle sources responsible for orogenic magmatism.

However, the behaviour of fluids under eclogite-facies conditions is not fully understood. At present, evidence is reported for both short and long-range migration. Circulation of high-pressure fluids at kilometre-scale is inferred from fluid-enhanced eclogitisation of dry granulites (e.g. Austrheim 1987; Austrheim and Engvik 1997; Austrheim et al. 1997; Jamtveit et al. 2000; Scambelluri et al. 1998) and from metasomatism of high-pressure rocks from ancient accretionary wedges (e.g. Sorensen and Grossman 1989; Bebout and Barton 1993; Nelson 1995). On the other hand, fluid inclusion and stable-isotope data from Alpine eclogites suggest that fluid flow was restricted under high-P conditions to millimetre- to decimetre-scales (e.g. Selverstone et al. 1992; Philippot 1993; Getty and Selverstone 1994; Philippot and Scambelluri 1995; Philippot et al. 1995; Scambelluri and Philippot 2001). In order to reconcile lack of pervasive fluid flow at eclogite-facies conditions with large-scale volatile transfer to the mantle wedge, Barnicoat and Cartwright (1995) also pointed out that fluid migration out of the subducting slab could be strongly channelled. Nevertheless, Zack et al. (2001) invoked pervasive, open-system flux of high-P fluids to explain homogenisation

of large ion lithophile elements in different eclogite-rock types from Trescolmen (Central Alps).

The analysis of vein systems can provide important constraints on fluid circulation in metamorphic terrains (e.g. Yardley and Bottrell 1992; Ague 1994a, 1994b; Cesare 1994; Oliver 1996; Oliver and Bons 2001). Large-scale circulation of disequilibrium fluids may cause metasomatic bands adjacent to the fluid channels (e.g. fractures, shear zones, layer boundaries) though such metasomatic effects do not necessarily require large mass-transport scales (Cesare 1994; Widmer and Thompson 2001). Disequilibrium fluids may not leave much evidence of their circulation under very fast flow rates or very low wallrock permeability. Mobile hydrofractures (fractures moving together with their contained fluid) can ascend rapidly over large distances with negligible effect on the country rocks until they are arrested due to the presence of obstacles, loss of fluid or unfavourable orientation. This is an efficient mechanism for fluid transport since the volume of fluid required to drive mobile hydrofractures is significantly lower than that needed for fluid flow in a connected fracture network (Oliver and Bons 2001).

Since the densities of hot fluids are less than those of cold fluids, fluid flow can occur along a temperature gradient if there is good connectivity and permeability. Therefore, large-scale fluid circulation may be an effective transport mechanism not only for mass but also for heat. However, thermo-mechanical models suggest that pervasive fluid flow cannot cause an appreciable thermal perturbation of the conductive geotherm, large fluxes and channelisation, typically related to fractures, shear zones or fold crests, are required (e.g. Bickle and McKenzie 1987; Brady 1988; Chamberlain and Rumble 1988; Oliver 1996; Connolly 1997; Thompson 1997).

The eclogite-facies terrain of the Marun-Keu (Polar Urals, Russia) offers a unique example to gain a different perspective on metasomatic processes at lower crustal depths. In this complex, Austrheim (1998) described eclogitisation of dry gabbros along fluid fronts, suggesting fluid migration of, at least, tens to hundred metre scales during the eclogite-facies metamorphism; Molina et al. (2002) report vein systems with well preserved wallrock alteration haloes.

In this work, we investigate blocks of amphibole-eclogites (in the sense of Liou et al. 1998) from the Marun-Keu complex in which pre-metasomatic assemblages are still preserved as relicts widespread through the metasomatic bands. Textural evidence for grain-scale, pore channelisation as described in experiments by Wark and Watson (2002) is reported for the first time in high-P vein-wallrock systems. Mass-balance calculations are performed for unravelling if chemical imbalances exist in the vein-wallrock system and, hence, for discussing the scale of mass transport during the growth of the amphibole-eclogite wallrock sequences. We also report for the first time very large temperature variations in high-pressure vein-wallrock systems discussing implications for large advective heat transport.

Geological setting of the Marun-Keu complex

The Marun-Keu complex in the Polar Urals (Russia) (approximately 67°N, 66°E) represents the northernmost high-P metamorphic complex of the Uralian Orogen (Udovkina 1971; Dobretsov and Sobolev 1984; Sobolev et al. 1986; Savelieva and Nesbitt 1996; Lennykh et al. 1997; Austrheim 1998; Molina et al. 2002).

This complex is a thrust sheet, with low-grade metasedimentary sequences of the Kharbei complex in the footwall, and oceanic and mantle rocks of the Syum–Keu ophiolite in the hanging wall (e.g. Udovkina 1971; Savelieva and Nesbitt 1996; Scarrow et al. 2001; Molina et al. 2002). The complex consists of Neoproterozoic to Cambrian volcanic-sedimentary sequences with mafic to felsic intrusive rocks (e.g. Udovkina 1971; Molina et al. 2002), which underwent eclogite-facies metamorphism at ~356 Ma (Glodny et al. 2003).

Our thermobarometric estimates (Molina et al. 2002) for the central and southern parts of the complex give temperatures ranging from 525 to 650 °C and pressures of ~14–17 kbar for the high-P event. In the northern part of the complex, lower temperature conditions are suggested by the presence of glaucophane metabasites, garnet-crossite quartzites and metagraywackes (Udovkina 1971; Dobretsov and Sobolev 1984; Sobolev et al. 1986).

Vein precipitates and wallrock amphibole-eclogite band sequences: textural analysis

A petrological assessment of mafic eclogites from Marun-Keu complex is available in Molina et al. (2002). This study focuses on a systematic mass-balance analysis of two representative samples (J-10 and PU-34) from the amphibole-eclogite sequences (see Table 1 for summary of mineral assemblages and textural features), which appear as decimetre-scale blocks included in a network of centimetre thick quartz-mica veins (Fig. 1a) (see also Fig. 3c in Molina et al. 2002).

Vein precipitates

The central part of the veins consists mostly of quartz and phengite. Towards the boundaries of the veins these minerals decrease in abundance with concomitant increases of predominantly garnet, with moderate amounts of omphacite and high-Al amphibole and minor paragonite, rutile and Cl-bearing apatite. Locally Cr-spinel appears as inclusions in omphacite grain cores. Garnet appears as large euhedral grains with minor inclusions of white mica, omphacite, high-Al amphibole, zoisite/clinozoisite and rutile. At the vein margins, large poikiloblasts of omphacite, with inclusions of garnet, high-Al amphibole, zoisite/clinozoisite and quartz, form a 2–5-mm-thick envelope.

The quartz in vein precipitates occurs in granoblastic aggregates suggesting it has recrystallised and, hence, the

Table 1 Textural features of amphibole-eclogite sequences form the Marun-Keu complex

Mineral zones	Mineral assemblage[a,b]	Texture
Vein centre	Q > Gar > Cpx, high-Al Amp > > Pheng Pg, Ru, Zo/Cz, Cl-Ap (All rims) (very rare Cr-Sp)	Locally, quartz and phengite may be very abundant in the central parts of the vein
Vein margin	Cpx > > Gar, Q > high-Al Amp > > Ru, Pg, Zo/Cz	Large poikiloblasts of clinopyroxene with inclusions of amphibole, garnet and quartz
Zone 1	Cpx > > high-Al Amp, Gar > > Ru, Py,	Clinopyroxene layer at the contact with the vein
Zone 2	Low-Al Amp > Cpx, Q, Ru, Py	Amphibole-rich mineral band with patches of relicts
Zone 3	Low-Al Amp > Cpx > Cc (after Arag?) > Q > > Ru, Py	Abundant amphibole and moderate calcite with patches of relicts
Relicts	(1) Cpx > Gar > > high-Al Amp > > Ru, Py, Pg, Cl-Ap	In patches through zones 2 and 3
	(2) High-Al Amp > Cpx > > Gar > > Ru, Py, Pg, Cl-Ap	In patches through zones 2 and 3

[a] *All* allanite; *Amp* amphibole; *Ap* apatite; *Arag* aragonite; *Cc* calcite; *Cpx* clinopyroxene; *Cr-Sp* Cr spinel; *Cz* clinozoisite; *Gar* garnet; *Pg* paragonite; *Pheng* phengite; *Q* quartz; *Py* pyrite; *Ru* rutile; *Zo* zoisite
[b] see Tables 5 and 6 for estimations of modal abundances

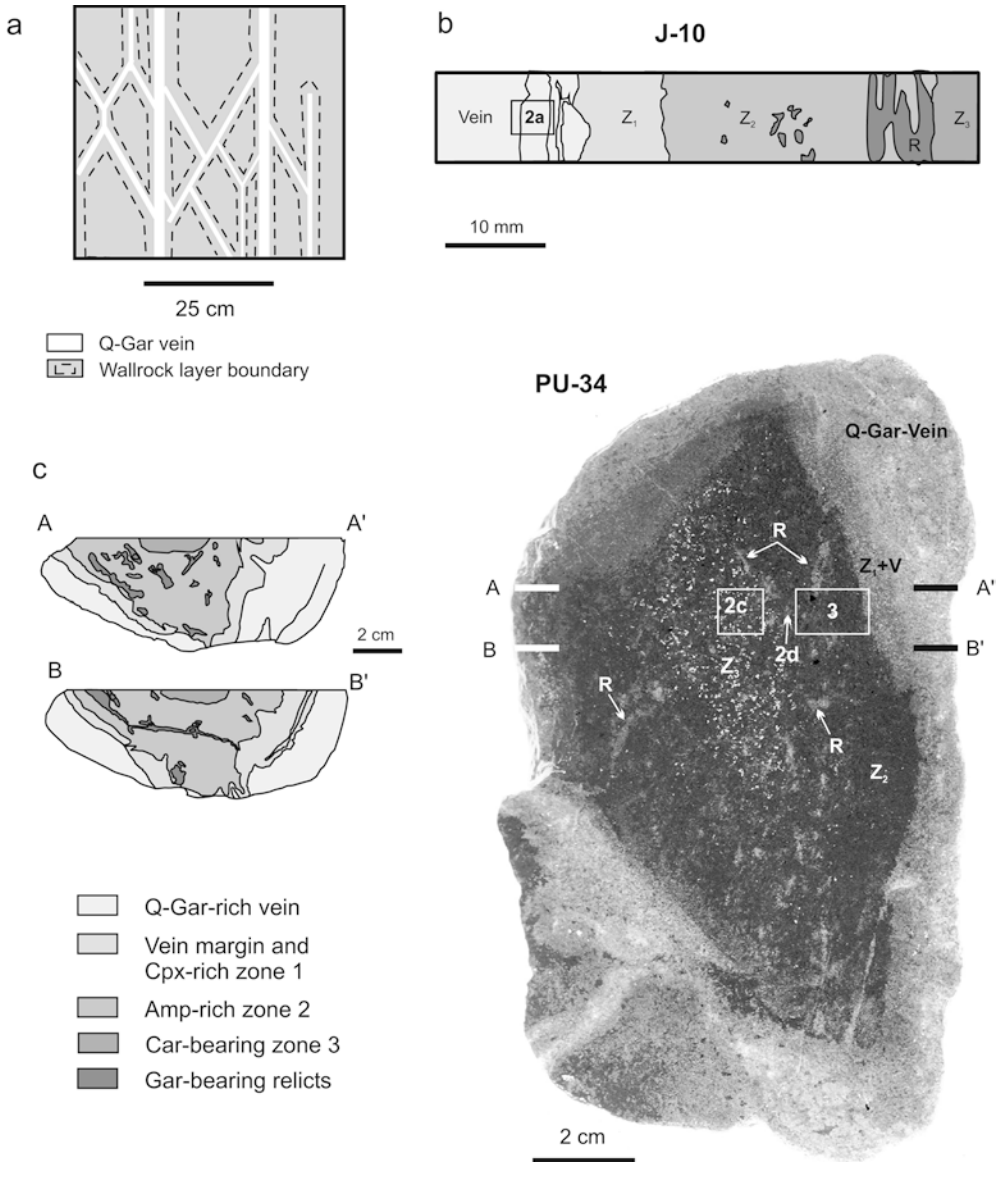

Fig. 1 a Schematic field relationships of high-P vein network with breccia-like structures in the Marun-Keu complex. Decimetre-scale blocks consisting of omphacite rich rinds and amphibolite cores are present inside the network. **b** Schematic relationships in sample J-10. Amphibole-eclogite sequence with patches of relicts across amphibole-rich zones 2. **c** Hand specimen (sample PU-34). Roughly concentric mineral band sequence with rinds of omphacite-rich zone 1 at the contact with quartz-garnet rich veins. Amphibole-rich zone 2 and carbonate-bearing zone 3 appear inwards. Note irregular patches and elongated lenses of relict assemblages across zones 2 and 3. Clinopyroxene veins crosscut the block (transect *B-B'*). *Insets* are location of BSE images and scan images from thin section in Figs. 2 and 3

original textural features of quartz in vein precipitates are probably lost. However, it is important to note the occurrence of tiny (10–100 μm) intergrowths of quartz-amphibole-garnet-zoisite/clinozoisite (Fig. 2a), quartz-phengite-zoisite/clinozoisite (Fig. 2b) and quartz-omphacite. Although their origin is uncertain, breakdown

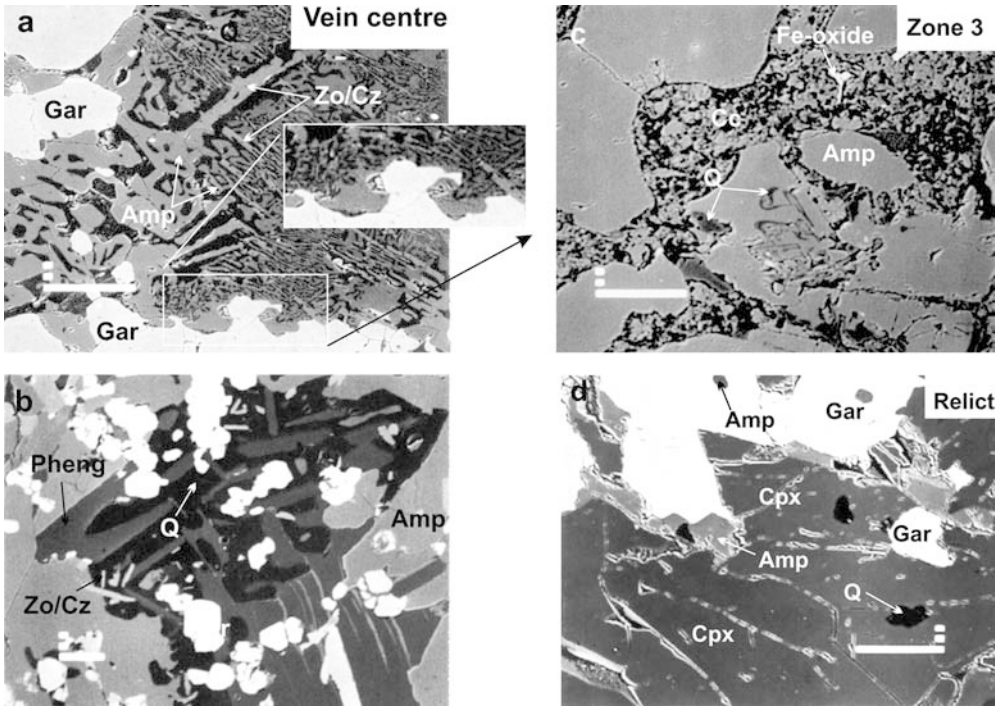

Fig. 2 Textural relationships in vein precipitates and wallrock assemblages. **a** BSE image of tiny intergrowths consisting of amphibole, quartz, zoisite/clinozoisite and phengite (not shown in the image) from a vein centre. Note straight grain boundaries of zoisite/clinozoisite. See Fig. 1b for image location. *Scale bar* 100 μm. **b** BSE image of tiny intergrowths of quartz and zoisite/clinozoisite and phengite from a vein crosscutting eclogites. *Scale bar* 100 μm. **c** BSE image of polycrystalline aggregate of calcite probably after aragonite in mineral zone 3. Note very tiny intergrowth of amphibole and quartz. See Fig. 1c for image location. *Scale bar* 100 μm. **d** BSE image of clinopyroxene-amphibole-garnet aggregate in relicts. Note sharp grain boundary at garnet-amphibole and garnet-clinopyroxene suggesting textural equilibrium. Note also grains of early amphibole included in garnet. See Fig. 1c for image location. *Scale bar* 100 μm

of early high-pressure mineral phases is unlikely due to: (1) the absence of pseudomorphic replacements or coronitic relations, (2) euhedral shapes of most phases in such aggregates (e.g. garnet, phengite and zoisite in Fig. 2a) and (3) intergrowths represents high-pressure assemblages themselves. Therefore, euhedrality of phases present in symplectitic intergrowths could suggest an eutectoid co-precipitation of such phases from the vein fluids.

Wallrock mineral sequence

Analysed amphibole-eclogite blocks display a roughly concentric mineral band sequence that parallels the vein, with the following mineral zones (Fig. 1b, c):

- Mineral zone 1 (Z_1): omphacite (>90 vol%) + garnet + aluminous amphibole.
- Mineral zone 2 (Z_2): low-Al amphibole + omphacite ± quartz.
- Mineral zone 3 (Z_3): low-Al amphibole + Na-rich diopside + calcite ± quartz.

Irregular patches of omphacite + garnet + high-Al amphibole are widespread across mineral zones 2 and 3 (Fig. 1b, c). These are interpreted to be the mineral assemblage prior to the metasomatic transformations (hereafter relict assemblages, **R**). Accessory rutile and pyrite are present in all these assemblages. Paragonite and Cl-bearing apatite can be present locally in the relicts.

Mineral zones 1 to 3 display a relict foliation defined by nematoblastic aggregates of amphibole and clinopyroxene. Locally, this foliation is replaced by decussate aggregates of amphibole and clinopyroxene (Fig. 3). This suggests that metasomatism occurred under static conditions, i.e. post-kinematic. Notably, the presence of a relict foliation in the omphacite-rich zone 1 contrasts with the large omphacite poikiloblasts observed in the margins of the vein. Therefore, this textural evidence strongly supports that the initial vein-wallrock boundary was located at the interface between these two omphacite-rich layers. In zone 3, calcite occurs in micrometer sized polycrystalline aggregates (Fig. 2c), which may suggest polymorphic transformation after aragonite (Liou et al. 1998).

The relicts present clinopyroxene-rich and amphibole-rich patches, with respectively: 60–70% Cpx, 30–40% Gar and 0–5% Amp; and 20–50% Cpx, 5–15% Gar and 50–70% Amp (by volume). In the clinopyroxene-rich patches, garnet-amphibole and garnet-clinopyroxene grain boundaries are sharp suggesting textural equilibrium (Fig. 2d). However, garnets from the amphibole-rich relicts (also locally in vein precipitate) present xenoblastic habits, and have been partially replaced by high-Fe amphibole at garnet-amphibole grain

boundaries and, to a lesser extent, garnet-clinopyroxene interfaces. The presence of such reaction rims in vein assemblages suggest that resorption of garnet occurred after original vein crystallization.

Three dimension estimates suggest that the volumes ((V^{Z_k})) of the mineral zones present the following relation: $V^{Z_2} > V^{Z_3} > V^{Z_1}$, with ratios $V^{Z_1}/V^{Z_2} = 0.1 - 0.3$ and $V^{Z_3}/V^{Z_2} = 0.3 - 0.7$.

Sample J-10 displays a complete rim-to-core sequence Z_1-Z_2-Z_3, with **R** widespread in zone 2 (Fig. 1b). PU-34 shows a more complex band organization (Fig. 1c): vein-Z_1-Z_2-Z_3-Z_2-vein with **R** in zones 2 and 3 (A-A' in Fig. 1c). At A, the vein margin displays abundant poikiloblastic amphibole and clinopyroxene: the clinopyroxene-rich layer at the block-vein contact seems elsewhere absent.

Quartz textures: the tracers of the intergranular fluids

In mineral zones 2 and 3, quartz is heterogeneously distributed as an interstitial phase. It is found along the grain boundaries of carbonate, amphibole and clinopyroxene (Fig. 3). It is important to note a tendency of interstitial quartz to coalesce in alignments roughly perpendicular to the boundary between mineral zones 1 and 2 (Fig. 3). Experiments by Wark and Watson (2002) indicate that rock pores may become aligned parallel to gradients in temperature or in composition of intergranular fluids (see Fig. 3b of Wark and Watson 2002). Accordingly, the alignment of interstitial quartz in the amphibole-eclogite sequences could be the result of a grain-scale, pore channelisation produced by compositional gradients through the intergranular fluid perpendicular to the reaction fronts. Because zone 3 is characterized by the presence of carbonates, gradients of fluid XCO_2 are most likely. Silica solubility in aqueous fluids increases with increasing temperature or pressure and with decreasing fluid XCO_2 (Newton and Manning 2000). If the intergranular fluid during metasomatism and vein growth was close to silica saturation, fluctuations in fluid XCO_2 could precipitate quartz, so providing a map of the pattern of fluid flow most relevant for mass transport. It is worth noting that despite modelling by Wark and Watson (2002) focused on quartz-dominated rocks, even more complex assemblages seem to develop channels on a similar time-scale (see below). Furthermore, as long as veining is pervasive on a decimetre scale, channelisation normal to the veins provides a way to promote ubiquitous interaction processes on a cm-mm scale.

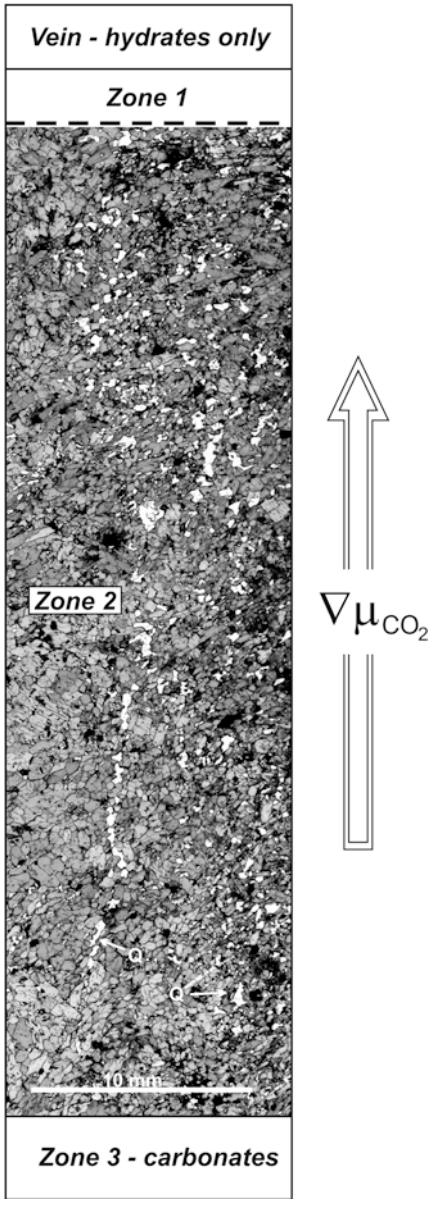

Fig. 3 Scan images from thin section with nematoblastic aggregate of amphibole and clinopyroxene from mineral zone 2. Note interstitial quartz along grain boundaries of clinopyroxene and amphibole grains locally coalescing to develop alignments at high angle to the boundary between mineral zones 1 and 2, which may provide evidence grain-scale channelisation of pores due to compositional gradients in the intergranular fluid as suggested by Wark and Watson (2002). See Fig. 1c for image location. *Scale bar* 10 mm

Mass imbalances during the growth of the eclogite-amphibolite wallrock sequence: evidence for an open system behaviour

Mineral chemistry

To determine the scale of equilibrium during the growth metasomatism and vein growth, a systematic survey of the mineral compositions of clinopyroxene, garnet and amphibole was performed on two profiles (Figs. 4 and 5) within samples J-10 and PU-34 (Tables 2, 3, 4; additional mineral chemistry data for the samples studied are also reported in Molina et al. 2002). Minerals were analysed by wavelength dispersive spectrometry with a Cameca Camebax electron microprobe at the Mineralogical-Geological Museum (University of Oslo) operated at 15 kV acceleration voltage and 20 nA beam current. Both natural and synthetic mineral standards

were employed for calibration. In order to minimize alkali loss, a defocused beam was employed for clinopyroxene analyses.

Pyroxene Clinopyroxene ranges from omphacite with 0.55–0.45 apfu Na unit (atoms per formula unit, based on 6 oxygen atoms) in veins, mineral zone 1, and relicts to Na-rich diopside with 0.35 apfu Na in zone 3 (Figs. 4a and 5a; Table 2). The Na and Al contents of clinopyroxene grains and continuously decrease from the vein, to Z_1, Z_2, to Z_3 whereas Ca increases. In contrast, the $Fe^{2+}/(Fe^{2+}+Mg)$ ratios of clinopyroxene show no correlation with the distance to the vein (Figs. 4a and 5a). Clinopyroxene inclusions in garnet show low $Fe^{2+}/(Fe^{2+}+Mg)$ ratios, whereas clinopyroxene matrix grains exhibit irregular zoning with rims showing both low and high $Fe^{2+}/(Fe^{2+}+Mg)$ ratios relative to cores (Table 2).

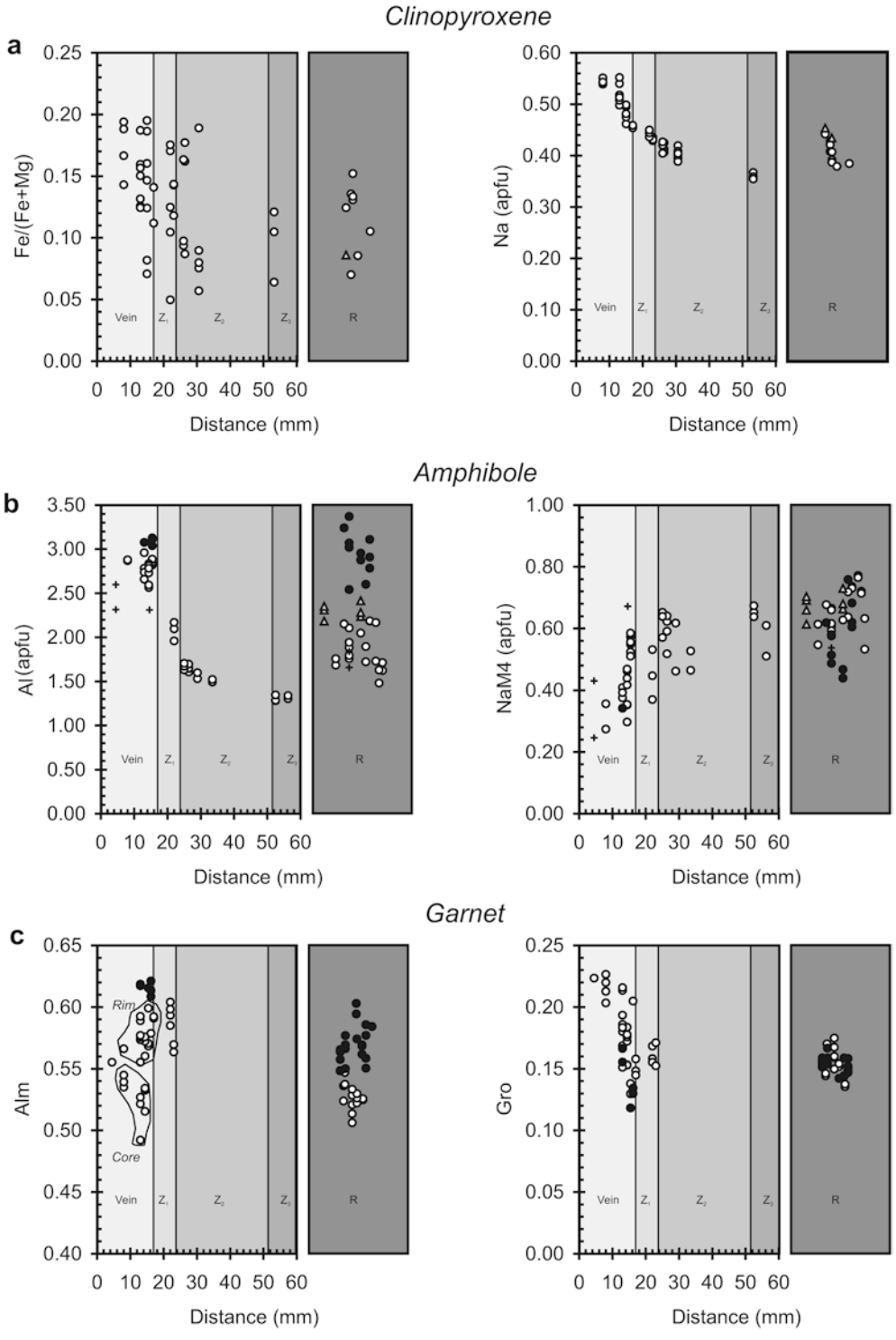

Fig. 4 Mineral composition in wallrock and vein assemblages from sample J-10 displayed against the distance to the centre of the vein. **a** Clinopyroxene composition. **b** Amphibole composition. **c** Garnet composition. Symbols: *open circle* unspecified mineral analyses (annotations are provided when systematic core-rim variations exist); *solid circle* resorption composition; *triangle* grain included in garnet; *cross* grain from quartz intergrowths. Unspecified location for analyses from relicts

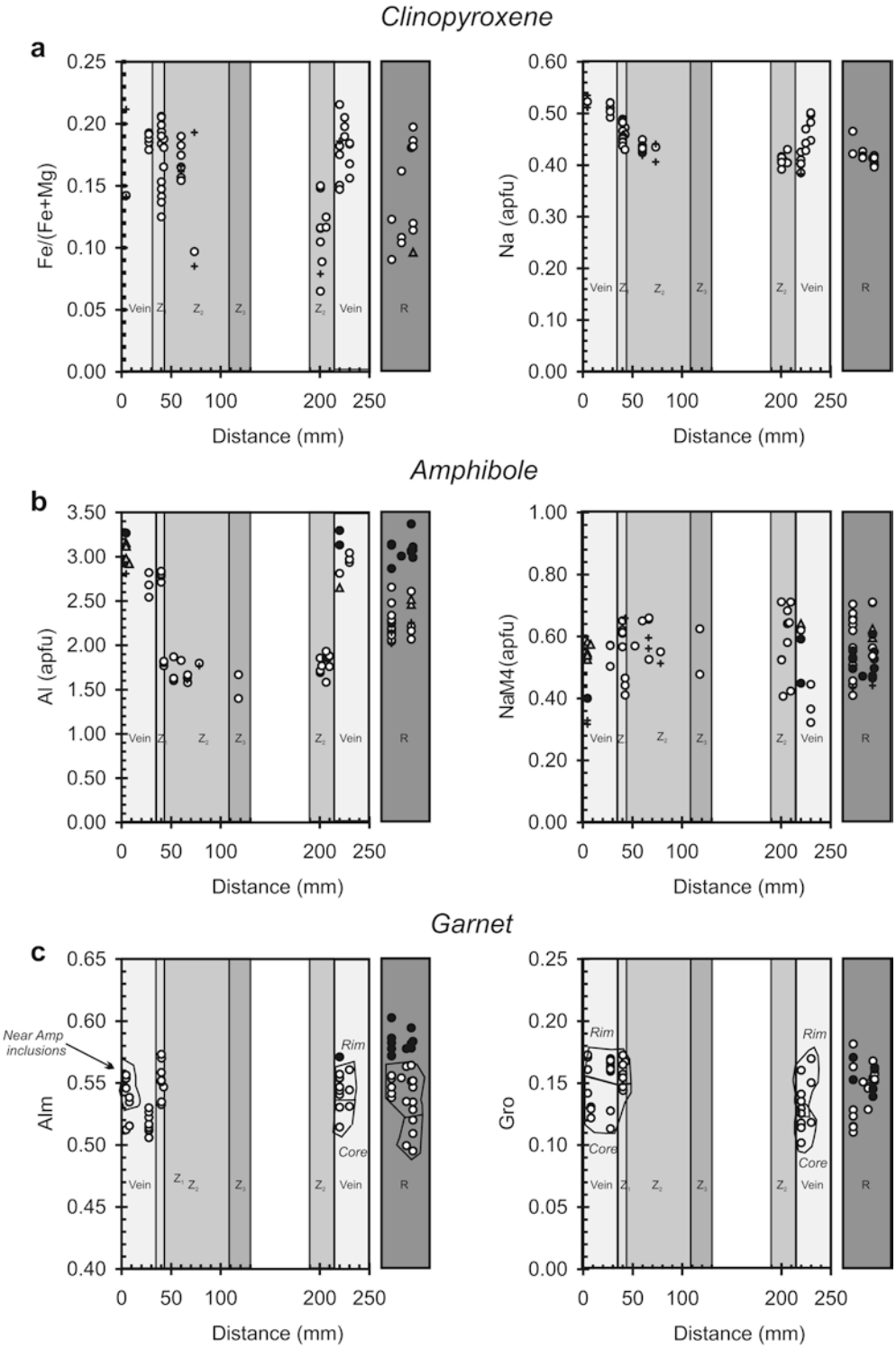

Fig. 5 Mineral composition in wallrock and vein assemblages from sample PU-34 displayed against the distance to the centre of the vein. **a** Clinopyroxene composition. **b** Amphibole composition. **c** Garnet composition. Symbols: *open circle* unspecified mineral analyses (annotations are provided when systematic core-rim variations exist); *solid circle* resorption composition; *triangle* grain included in garnet; *cross* grain from quartz intergrowths. Unspecified location for analyses from relicts

Amphibole Most compositions ranges mostly from pargasite and edenite with 0.25 to 0.50 apfu Na^{M4} (based on 23 atoms of oxygen, assuming that sum of cations –Ca–Na–K = 13) in veins, in Z_1 and **R**, to magnesiotaramite and magnesiokatophorite with 0.51–0.77 apfu Na^{M4} in Z_2 and Z_3 (Figs. 4b and 5b, Table 3). Minor barroisite, with 0.51 to 0.81 apfu Na^{M4} is also present in the two samples. Magnesiohornblende grains occur as inclusions in poikiloblastic omphacite from PU-34. Chlorine in amphibole from PU-34 ranges from ~0.03 to 0.22 apfu, with the largest values in vein amphibole (Molina et al. 2002).

Amphibole grains from the veins display larger Al, Na^{A} and $Fe^{2+}/(Fe^{2+}+Mg)$ ratios, and smaller Na^{M4} than that from metasomatic assemblages (Table 3). As for clinopyroxene, amphibole compositions across the

Table 2 Representative clinopyroxene compositions (normalised to 6 atoms of oxygen)

Sample	PU34	J10	PU34	PU34	PU34	PU34	J10	J10	J10	PU34	PU34	PU34
Label	A24	219	A22b	A10c	A13b	A6	156	168	160	C7	C3b	C2b
Zone	V.C.	V.C	V.M.	Z1	Z1	Z2	Z2	Z3	R	R	R	R
Texture	Core	Core	Core	Core	Rim	Core	Core	Core	Gar-inc	Core	Rim	Rim
SiO_2	55.62	55.44	55.95	56.47	56.62	56.30	54.29	54.83	55.21	55.38	56.09	55.34
TiO_2	0.12	0.28	0.13	0.18	0.20	0.18	0.23	0.08	0.22	0.15	0.10	0.13
Al_2O_3	12.66	11.95	11.92	11.55	10.39	9.11	8.16	6.08	9.05	8.96	9.41	8.96
Cr_2O_3	0.04	1.79	0.30	0.09	0.29	0.22	0.25	0.37	0.07	0.20	0.19	0.00
NiO	0.05	0.03	0.11	0.00	0.06	0.01	0.00	0.06	0.01	0.03	0.15	0.00
FeO_t	3.68	4.97	3.87	3.90	3.90	4.34	6.11	6.50	5.69	4.98	4.91	4.77
MnO	0.00	0.00	0.03	0.03	0.08	0.05	0.00	0.12	0.10	0.09	0.03	0.17
MgO	7.53	6.52	7.76	8.37	8.80	9.29	9.52	10.45	8.64	9.57	9.53	9.82
CaO	12.06	11.54	12.97	13.42	14.19	14.90	15.60	16.87	14.62	15.03	14.58	15.38
Na_2O	7.60	8.03	7.18	6.83	6.39	6.17	5.85	5.16	6.56	6.01	5.90	5.74
K_2O	0.08	0.02	0.00	0.00	0.01	0.02	0.01	0.00	0.02	0.02	0.01	0.01
Total	99.45	100.58	100.23	100.84	100.94	100.60	100.03	100.52	100.21	100.42	100.91	100.32
Si	1.973	1.962	1.979	1.987	1.998	1.996	1.945	1.965	1.967	1.969	1.986	1.970
Ti	0.003	0.007	0.004	0.005	0.005	0.005	0.006	0.002	0.006	0.004	0.003	0.004
Al	0.529	0.499	0.497	0.479	0.432	0.381	0.345	0.257	0.380	0.375	0.393	0.376
Cr	0.001	0.050	0.008	0.002	0.008	0.006	0.007	0.010	0.002	0.006	0.005	0.000
Ni	0.001	0.001	0.003	0.000	0.002	0.000	0.000	0.002	0.000	0.001	0.004	0.000
Fe_t	0.109	0.147	0.115	0.115	0.115	0.129	0.183	0.195	0.169	0.148	0.146	0.142
Mn	0.000	0.000	0.001	0.001	0.002	0.002	0.000	0.004	0.003	0.003	0.001	0.005
Mg	0.398	0.344	0.409	0.439	0.463	0.491	0.508	0.558	0.459	0.507	0.503	0.521
Ca	0.458	0.438	0.491	0.506	0.536	0.566	0.599	0.648	0.558	0.572	0.553	0.586
Na	0.523	0.551	0.492	0.466	0.437	0.424	0.406	0.359	0.454	0.414	0.405	0.396
K	0.004	0.001	0.000	0.000	0.001	0.001	0.001	0.000	0.001	0.001	0.001	0.001
Fe^{3+}	0.045	0.064	0.022	0.001	0.000	0.037	0.153	0.157	0.126	0.089	0.030	0.075
Fe^{2+}	0.065	0.083	0.093	0.114	0.115	0.091	0.030	0.038	0.043	0.059	0.115	0.067
$Fe^{2+}/(Fe^{2+}+Mg)$	0.140	0.194	0.185	0.205	0.199	0.157	0.056	0.064	0.086	0.104	0.186	0.114

metasomatic mineral bands continuously decrease in Al, Na^A and $Fe^{2+}/(Fe^{2+}+Mg)$ from the vein to Z_3 (Figs. 4b and 5b; Table 3).

In **R**, amphibole inclusions in garnet exhibit the smallest average $Fe^{2+}/(Fe^{2+}+Mg)$ atomic ratios (0.16 to 0.22) and the greatest Na^{M4} contents (0.61 to 0.73 apfu). Amphibole that has replaced garnet contains 2.60 to 3.37 Al apfu and 0.61 to 0.86 Na^A apfu with $Fe^{2+}/(Fe^{2+}+Mg)$ of 0.29 to 0.39.

Garnet Garnet compositions are almandine-rich ($Alm_{50–65}$), contain with moderate amounts of pyrope ($Pyr_{17–35}$) and grossular ($Gro_{12–23}$) and are poor in spessartine ($Sps_{1–9}$). In relict assemblages, small garnet inclusions in clinopyroxene and the cores of large garnet grains show the smallest almandine contents ($Alm_{50–53}$). Partially resorbed garnet is richer in almandine ($Alm_{55–65}$) and poorer in pyrope ($Pyr_{17–25}$) (Table 4). Spessartine varies sympathetically with almandine, exhibiting marked variations due to the resorption process. Small partially resorbed garnet grains (a few tens of microns) contain the most spessartine ($Sps_{7–9}$); larger garnet grains, inverse Mn zoning ranges from 3 mol% spessartine in the core to 8 mol% in the resorption rims of a single grain. In contrast, grossular contents of garnet from relict assemblages shows no systematic variations related to resorption (Figs. 4c and 5c).

The composition of garnet in veins assemblages is variable. In general, resorption rims contain the highest almandine ($> Alm_{57}$). In sample J-10, garnet from the central part of the vein shows only minor variations in pyrope, grossular and spessartine contents with no systematic core to rim relationships. A slight increase in almandine component is seen in grain rims (Table 4), at $Gro_{20–23}$, these are the Ca-richest garnets. The core compositions of garnet inclusions in clinopyroxene at vein margins are depleted in almandine and spessartine and enriched in pyrope relative to rims. Garnet aggregates nearest the vein margins may represent local overgrowths, because these are rich in grossular. It will be shown later that garnet rim compositional differences are unrelated to temperature differences, suggesting that the grossular-rich overgrowths should be ascribed to variations of the effective bulk composition of the vein.

In the vein assemblages of PU-34, both rim and core compositions of garnet grains show $Alm_{50–53}$, with $Alm_{53–57}$ close to inclusions of amphibole. Grossular contents vary systematically from $Gro_{11–14}$ in cores to $Gro_{14–18}$ in rims.

Mass-balance

The purpose of this section is to assess if mass balance requires the introduction of chemical components from the vein fluids, and hence to discuss whether these veins were produced by local segregation or they require large-scale mass transport. If all components were released from the wallrock (one way mass-transfer), the vein

Table 3 Representative amphibole compositions (normalised to 23 atoms of oxygen)

Sample	PU34	J10	PU34	J10	PU34	J10	PU34	PU34	PU34	J10	PU34	J10	J10	PU34	J10	J10
Label	A26b	215	A18	261	A15b	153	B17	A11b	A4b	159	B11	137	130	C9b	111	125
Zone	V.C.	V.C.	V.M.	V.M.	Z1	Z1	Z2	Z2	Z2	Z2	Z3	Z3	R	R	R	R
Texture	Gar-inc	Rim	Core	Core	Core	Core	Core	Q-inter	Rim	Core	Core	Core	Core	Gar-inc	Res	Rim
SiO_2	40.54	43.90	48.56	45.24	46.68	46.38	50.38	50.25	47.36	49.59	50.36	51.15	48.75	46.91	40.62	49.01
TiO_2	0.05	0.58	0.18	0.50	0.15	0.55	0.63	0.53	0.48	0.45	0.45	0.48	0.45	0.25	0.37	0.32
Al_2O_3	18.12	16.89	13.53	15.27	16.97	12.23	9.66	10.85	10.69	9.01	8.31	7.78	13.87	14.78	19.48	7.90
Cr_2O_3	0.00	0.38	0.07	0.06	0.15	0.10	0.26	0.00	0.19	0.13	0.37	0.10	0.12	0.22	0.18	0.04
NiO	0.00	0.01	0.00	0.19	0.11	0.08	0.00	0.05	0.08	0.05	0.00	0.00	0.01	0.01	0.00	0.00
FeO_t	15.08	10.91	9.55	10.72	8.75	11.51	8.37	8.08	8.43	8.63	7.62	9.62	7.38	10.29	12.35	8.97
MnO	0.17	0.03	0.22	0.10	0.01	0.08	0.08	0.08	0.10	0.17	0.09	0.18	0.04	0.01	0.19	0.18
MgO	8.89	11.04	13.23	11.84	12.34	12.29	15.30	14.34	15.01	15.14	15.97	15.85	14.36	12.52	9.43	15.40
CaO	9.30	10.69	10.06	9.99	9.18	9.96	8.26	9.07	10.27	10.05	9.95	8.81	8.83	9.08	9.44	10.47
Na_2O	4.19	3.38	3.45	3.68	4.46	3.63	4.04	3.91	3.29	3.59	3.13	4.03	4.54	3.98	4.50	3.05
K_2O	0.31	0.42	0.05	0.34	0.17	0.37	0.72	0.61	0.46	0.43	0.29	0.58	0.57	0.45	0.77	0.24
Total	96.65	98.24	98.90	97.93	98.96	97.17	97.71	97.77	96.36	97.24	96.53	98.60	98.92	98.50	97.34	95.57
Si	5.993	6.326	6.817	6.498	6.545	6.747	7.093	7.107	6.838	7.109	7.191	7.181	6.803	6.630	5.963	7.142
Ti	0.006	0.063	0.019	0.054	0.016	0.060	0.067	0.057	0.053	0.049	0.048	0.051	0.047	0.027	0.041	0.035
Al	3.158	2.869	2.239	2.585	2.804	2.096	1.602	1.808	1.820	1.523	1.399	1.288	2.281	2.462	3.371	1.357
Cr	0.000	0.043	0.008	0.007	0.016	0.012	0.029	0.000	0.022	0.015	0.041	0.011	0.013	0.024	0.020	0.005
Ni	0.000	0.001	0.000	0.022	0.013	0.009	0.000	0.006	0.009	0.006	0.000	0.000	0.001	0.001	0.000	0.000
Fe_t	1.864	1.315	1.121	1.287	1.026	1.401	0.986	0.956	1.017	1.035	0.910	1.130	0.862	1.216	1.516	1.093
Mn	0.021	0.003	0.026	0.013	0.002	0.010	0.009	0.009	0.013	0.020	0.011	0.021	0.005	0.002	0.024	0.022
Mg	1.959	2.372	2.769	2.535	2.579	2.665	3.212	3.024	3.229	3.235	3.399	3.317	2.987	2.638	2.065	3.346
Ca	1.474	1.651	1.513	1.537	1.379	1.553	1.245	1.374	1.589	1.543	1.522	1.326	1.320	1.375	1.486	1.634
Na	1.202	0.945	0.939	1.025	1.213	1.023	1.104	1.072	0.921	0.997	0.866	1.097	1.229	1.090	1.282	0.861
K	0.059	0.078	0.009	0.062	0.030	0.069	0.130	0.111	0.084	0.079	0.053	0.104	0.101	0.080	0.144	0.045
Fe^{3+}	0.637	0.000	0.104	0.143	0.057	0.078	0.323	0.000	0.196	0.000	0.117	0.384	0.034	0.280	0.204	0.111
Fe^{2+}	1.228	1.315	1.016	1.144	0.969	1.323	0.664	0.956	0.821	1.035	0.792	0.745	0.828	0.937	1.312	0.982
Al^{IV}	2.007	1.674	1.183	1.502	1.455	1.253	0.907	0.893	1.162	0.891	0.809	0.819	1.197	1.370	2.037	0.858
Al^{VI}	1.151	1.195	1.056	1.083	1.349	0.844	0.696	0.915	0.657	0.632	0.591	0.469	1.085	1.092	1.334	0.499
Na^{M4}	0.526	0.357	0.487	0.463	0.621	0.447	0.755	0.659	0.411	0.465	0.478	0.674	0.680	0.625	0.514	0.366
Na^{A}	0.676	0.589	0.453	0.562	0.592	0.576	0.350	0.413	0.509	0.532	0.388	0.423	0.549	0.465	0.767	0.495
$Fe^{2+}/(Fe^{2+}+Mg)$	0.385	0.357	0.268	0.311	0.273	0.332	0.171	0.240	0.203	0.242	0.189	0.183	0.217	0.262	0.389	0.227

formation is consistent with a mechanism of local segregation. On the contrary, if some component must be added to transform the starting rock into the metasomatic layer (two way mass-transfer), a long-range (probably at least >metre scale) mass-transport and fluid-circulation is required.

To achieve this purpose, mass-balance calculations are performed between relicts, which could be an approach of the protolith, and the mineral zones 1 to 3. Such a boundary condition is safely assumed on the basis of remnants of a relic foliation (see section on textural analysis) which suggests that the original vein/wallrock interface was located between Z_1 and the clinopyroxene-rich layer on the margin of the vein. Then, we will calculate the following relation for i^{th} chemical component:

$$m^R C_i^R + \Delta m_i = \sum_{k=1}^{k=3} m^{Z_k} C_i^{Z_k} \quad (1)$$

where m^{Z_k} and m^R are, respectively, the molar masses of the k^{th} metasomatic layers and the relict, Δm_i is molar mass imbalance of the i^{th} chemical component, and $C_i^{Z_k}$ and C_i^R are the molar concentration of the i^{th} chemical component in the k^{th} metasomatic layers and the relict, respectively.

For using relation (1), it is necessary to determine the composition and masses of wallrock mineral layers and relict and to establish a reference frame based on, if any, a conserved magnitude. It is important to note that composition of vein precipitates is not required.

Compositional system and bulk chemistry of wallrock layers

Direct sampling and determination of the bulk composition of individual mineral zones and relicts is hampered when veining and metasomatism are pervasive, i.e. distributed on a mm-cm scale (see description of 3D pattern in Fig. 1). The protolith is heterogeneously distributed in mm-size relic domains and we showed that mass-transfer is also controlled by channelled pores. As a result, a careful selection of microstructural domains is critical to correctly evaluate silica distribution as well as other mobile components and the processes outlined here closely resemble mass-transfer in coronas/symplectites rather than conventional vein/wallrock geometries.

Bulk compositions are therefore evaluated from phase abundances and composition of mineral phases (Table 5). The approach adopted here is a simplification

Table 4 Representative garnet compositions (normalised to 12 atoms of oxygen)

Sample	PU34	PU34	J10	PU34	J10	J10	J10	J10	PU34	J10	J10	PU34	J10	PU34	J10	J10
Label	A14c	A20	218	A24b	23	24	27	264	A8c	13	241	C7b	114	C14b	178	117
Zone	V.C.	V.C.	V.C.	V.M.	V.M.	V.M.	V.M.	V.M.	Z1	Z1	Z1	R	R	R	R	R
Texture	Core	Rim	Rim	Core	Core	Rim	Rim	Res	Core	Core	Rim	Core	Core	Res.	Res	Rim
SiO_2	39.26	38.95	38.78	39.53	38.78	38.50	38.40	38.78	38.70	38.53	38.03	39.53	39.08	38.74	38.70	39.21
TiO_2	0.03	0.17	0.08	0.08	0.07	0.05	0.03	0.03	0.03	0.10	0.12	0.05	0.07	0.00	0.00	0.08
Al_2O_3	21.74	21.62	21.26	21.64	21.26	21.46	20.69	21.33	21.56	21.03	21.03	21.81	21.18	21.22	21.33	21.37
Cr_2O_3	0.10	0.13	0.42	0.25	0.20	0.13	0.59	0.01	0.28	0.35	0.29	0.00	0.28	0.38	0.10	0.19
NiO	0.00	0.00	0.01	0.06	0.03	0.08	0.08	0.00	0.04	0.00	0.09	0.00	0.05	0.00	0.11	0.00
FeO_t	24.84	23.85	25.14	24.08	24.96	25.93	26.68	28.73	26.87	26.78	27.57	23.53	24.64	27.27	27.45	23.93
MnO	0.66	0.36	0.74	0.88	0.80	0.84	1.15	1.27	1.12	1.15	1.27	1.05	0.97	1.77	2.88	1.08
MgO	9.42	8.32	5.70	9.29	7.89	6.45	4.78	6.25	7.64	6.18	5.85	8.54	8.26	6.33	5.70	7.84
CaO	4.59	5.85	8.24	4.14	6.25	6.57	7.81	4.31	4.30	6.28	5.75	6.02	5.96	5.09	4.41	6.45
Na_2O	0.00	0.01	0.04	0.03	0.00	0.03	0.05	0.05	0.00	0.00	0.04	0.03	0.04	0.04	0.03	0.07
K_2O	0.00	0.02	0.00	0.00	0.00	0.00	0.02	0.00	0.00	0.01	0.02	0.01	0.01	0.00	0.00	0.00
Total	100.64	99.29	100.42	99.98	100.24	100.03	100.29	100.77	100.54	100.42	100.07	100.56	100.54	100.85	100.72	100.23
Si	2.993	3.007	3.007	3.022	2.992	2.995	3.012	3.015	2.989	3.000	2.986	3.013	3.002	3.006	3.016	3.014
Ti	0.002	0.010	0.005	0.005	0.004	0.003	0.002	0.002	0.002	0.006	0.007	0.003	0.004	0.000	0.000	0.005
Al	1.953	1.967	1.943	1.950	1.933	1.967	1.913	1.954	1.963	1.930	1.946	1.959	1.918	1.941	1.960	1.937
Cr	0.006	0.008	0.026	0.015	0.012	0.008	0.037	0.001	0.017	0.022	0.018	0.000	0.017	0.023	0.006	0.012
Ni	0.000	0.000	0.001	0.004	0.002	0.005	0.005	0.000	0.002	0.000	0.006	0.000	0.003	0.000	0.007	0.000
Fe_t	1.583	1.540	1.630	1.540	1.610	1.687	1.751	1.867	1.736	1.744	1.810	1.500	1.583	1.770	1.790	1.538
Mn	0.043	0.024	0.048	0.057	0.052	0.056	0.076	0.083	0.074	0.076	0.084	0.068	0.063	0.116	0.190	0.071
Mg	1.071	0.958	0.659	1.058	0.908	0.748	0.559	0.724	0.880	0.718	0.685	0.970	0.946	0.733	0.663	0.899
Ca	0.374	0.484	0.685	0.339	0.517	0.547	0.657	0.359	0.356	0.524	0.484	0.491	0.491	0.423	0.368	0.531
Alm	0.515	0.512	0.539	0.514	0.522	0.555	0.575	0.616	0.570	0.570	0.591	0.495	0.514	0.582	0.594	0.506
Sps	0.014	0.008	0.016	0.019	0.017	0.018	0.025	0.027	0.024	0.025	0.027	0.022	0.020	0.038	0.063	0.023
Pyr	0.349	0.319	0.218	0.353	0.294	0.246	0.184	0.239	0.289	0.234	0.224	0.320	0.307	0.241	0.220	0.296
Gro	0.122	0.161	0.227	0.113	0.167	0.180	0.216	0.118	0.117	0.171	0.158	0.162	0.159	0.139	0.122	0.175

of the procedure proposed by Ashworth and Birdi (1990) for the modelling of open system behaviour during corona growth in metagabbros. Similarly, mass fluxes and phenomenological diffusion coefficients were retrieved in a variety of petrological problems (e.g. Jamtveit et al. 1990; Ashworth and Sheplev 1997; Godard and Martin 2000).

Calculations are performed in the model system Na-Ca-Mg-Fe-Al-Si-H-C-O. Ti, Mn, Cl and K were neglected as they show very low contents in the wallrock assemblages. Contents in oxygen, carbon and hydrogen were obtained by stoichiometry as O-OH substitution in amphibole is unlikely in this type of environment. Mineral abundances were estimated from point counting in thin sections and BSE images. In order to evaluate the influence of grain-scale and pore channelisation on the estimates of bulk composition, we performed calculations for both quartz-rich and quartz-poor domains in Z_2 and Z_3.

In order to evaluate the actual influence of uncertainties in metasomatic zone compositions, we propagated uncertainties using the Monte Carlo method (Anderson 1976) from uncertainties in composition and abundance of mineral phases, considering a relative error up to ca. 5%. Relative errors in the estimated compositions are better than ca 8% for 3–7 mol%, 5% for 15–20 mol% and 2% for ca. 60 mol% (Table 5). Significant compositional differences, which may be attributed to grain-scale, pore channelisation, are observed in mineral zone 3 with relative variations of ca. 17 mol% in Ca and 9 mol% in Si; whereas in mineral zone 2, these are negligible within the uncertainties (relative variation of ca. 3 mol% in Si, Al, Fe and Mg; and ca. 4 mol% in Na and Ca). It is interesting to note that oxygen variations are negligible in the two mineral zones (relative variation < 0.6 mol%).

Reference frame

The variations of chemical components in rocks experiencing metasomatism must be measured with respect to some specific frame of reference (e.g. Thompson 1959; Gresens 1967; Brady 1975; Thompson 1975). Thus, if a component u is selected as reference frame, the relative movement of the other components is measured with respect to the velocity of component u. In general, it is desirable to choose as a reference frame some quantity, which is conserved during the metasomatic process or, at least, exhibits the lowest velocity (otherwise, although valid, a complex description of the component variations may arise; see Thompson 1975).

Appropriate reference-frames for evaluating mass changes during metasomatism can be chosen using the method of the isocon of Grant (1986), which is based on the equations derived by Gresens (1967). This method has been proved to be robust in evaluating mass transformations in a multitude of geological problems (most recently Cail and Cline 2001; Nijland and Touret 2001; Widmer and Thompson 2001; Markl et al. 2003; Altaner

Table 5 Bulk composition estimations of mineral bands from amphibole-eclogite sequences from the Marun-Keu complex[a, b,c]

Zone	1		2		2		3		3	
Domain			Q-free		Q-bearing		Q-free		Q-bearing	
	mean	1σ	mean	1σ	mean	1σ	mean	1σ	mean	1σ
Modal mineral abundance (by volume)										
Amp	0.04	0.03	0.73	0.02	0.71	0.02	0.68	0.03	0.67	0.03
Gar	0.02	0.02	-	-	-	-	-	-	-	-
Cpx	0.94	0.02	0.27	0.04	0.24	0.04	0.20	0.02	0.20	0.02
Q	-	-	tz	-	0.06	0.02	tz	-	0.08	0.02
Cc	-	-	-	-	-	-	0.11	0.02	0.05	0.02
Estimated mineral band compositions (molar fraction)										
Si	0.1947	0.0081	0.1773	0.0062	0.1844	0.0060	0.1600	0.0064	0.1813	0.0065
Al	0.0397	0.0021	0.0395	0.0020	0.0378	0.0018	0.0265	0.0012	0.0262	0.0012
Fe	0.0197	0.0016	0.0217	0.0010	0.0207	0.0010	0.0231	0.0011	0.0227	0.0011
Mg	0.0489	0.0027	0.0677	0.0032	0.0648	0.0030	0.0661	0.0031	0.0652	0.0031
Ca	0.0533	0.0034	0.0452	0.0018	0.0427	0.0018	0.0560	0.0028	0.0440	0.0028
Na	0.0417	0.0029	0.0267	0.0013	0.0251	0.0013	0.0258	0.0013	0.0254	0.0013
H	0.0020	0.0012	0.0344	0.0026	0.0335	0.0025	0.0332	0.0020	0.0328	0.0020
C	-	-	-	-	-	-	0.0203	0.0024	0.0087	0.0029
O	0.5987	0.0100	0.5851	0.0103	0.5888	0.0099	0.5864	0.0091	0.5912	0.0089
ρ	0.1583	0.0086	0.1498	0.0093	0.1487	0.0091	0.1475	0.0074	0.1468	0.0074

[a]Mineral density values employed in bulk composition estimations (mole/cm^3): Low-Al amp, 0.1457; High-Al amp, 0.1604; Gar, 0.1716; Cpx, 0.1572; Q, 0.1313; Cc, 0.1354

[b]Uncertainties in mineral densities for solid solution minerals: 1.8–4.7%

[c]H, C and O contents calculated by stoichiometry

et al. 2003; Selverstone and Hyatt 2003; Yonkee et al. 2003). A brief summary of this treatment is described in the Appendix. Isocons through the origin, as indicated by relation A4 in Appendix, were fitted by least-square methods for all the components clustering around the total molar-mass isocon and also excluding silicon and oxygen for evaluating the influence of major components. Baumgarter and Olsen (1995) proposed an improvement of the isocon method by x-y weighted least-square procedures. Testing the calculation suggested by Baumgartner and Olsen (1995) versus the fitted isocons as described previously results in differences of a few permills in correlation coefficients. Consequently, the results obtained were considered to be robust within the bulk composition uncertainties.

Isocon diagrams for adjacent mineral zones from the amphibole-eclogite sequence show that, at least, three components, which include iron and oxygen in all cases, plot very close to the total molar-mass isocon (filled symbols in Fig. 6a, b), suggesting that their mass variations were negligible with respect to a total molar-mass reference-frame (within ±3%).

Model bulk chemistry of relicts

Since the abundance of amphibole and clinopyroxene in the relicts is variable, model bulk compositions for relicts have been estimated by mass-balance calculations, assuming an assemblage consisting of high-Al amphibole, garnet and clinopyroxene. Calculations were performed assuming the conservation of the total molar mass, oxygen and iron as previously discussed, using average contents of 59.00 mol% O and 2.16 mol% Fe, with amphibole, garnet and clinopyroxene compositions reported for relicts (resorption compositions were avoided). The estimated mineral abundances along with the derived relict compositions are listed in Table 6. Abundances for amphibole and clinopyroxene in the model relict are high with values of ca 42 and 55 mol%, respectively.

Mass imbalance estimates

For a reference frame conserving the total molar-mass, the following relation between the molar masses of metasomatic layers m^{Z_k} and the relict m_R holds:

$$m^R - \sum_{k=1}^{k=3} m^{Z_k} = 0 \tag{2}$$

in which m_R can be fixed to an arbitrary value.

Therefore, there are three m^{Z_k} unknowns and one constraint imposed by relation (2). However, two additional constraints are imposed by ratio of volumes of product layers:

$$r_{12} = \frac{V^{Z_1}}{V^{Z_2}} \tag{3a}$$

$$r_{32} = \frac{V^{Z_3}}{V^{Z_2}} \tag{3b}$$

where r_{12} and r_{32} are obtained by inspection.

Fixing $m_R = 100$ in relation (2), substituting V^{Z_k} by m^{Z_k}/ρ^{Z_k} (where ρ^{Z_k} is the molar density of the k^{th} layer)

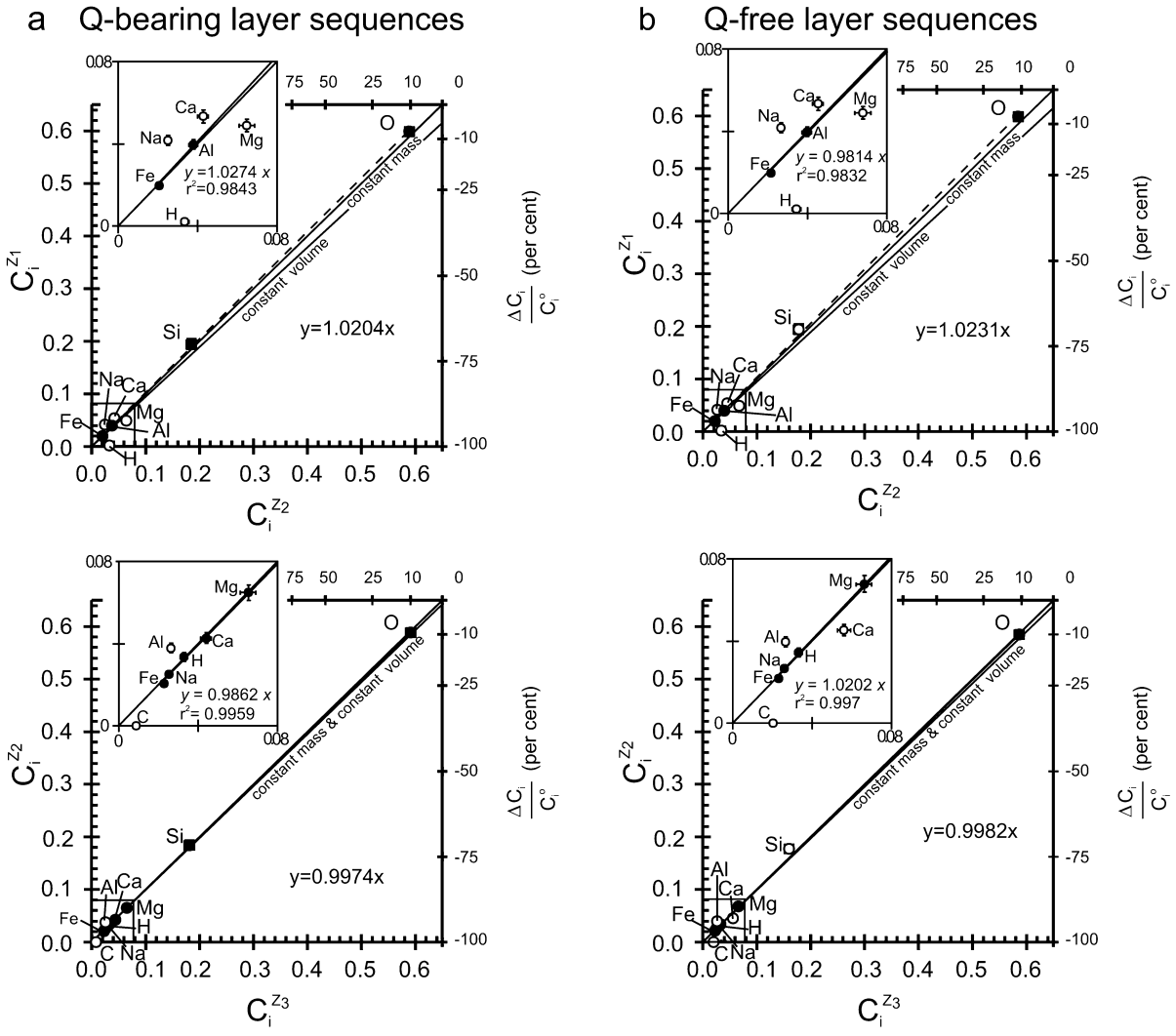

Fig. 6 Isocon diagrams for mineral zones 1, 2 and 3, employing molar concentration normalized to one as listed in Table 5. **a** Quartz-bearing domains. **b** Q-free domains. Isocon lines calculated by least-square regression methods are also plotted in the diagram along with isocon equations; square of correlation coefficient (r^2) is better than 0.9999. *Solid circles* are components employed for isocon calculations. Isocons for constant total molar mass and volume are also shown. *Insets* are isocon diagrams with isocons fitted excluding silicon and oxygen. Note closeness of fitted isocons to that for conservation of total molar mass. Note also negligible influence of silicon and oxygen on the regressed isocons. See text for discussion and for bulk composition estimations of mineral zones

in relations (3a, 3b), and solving for m^{Z_k}, the molar mass of k^{th} layer produced during the consumption of 100 moles of starting rock is obtained:

$$m^{Z_k} = \frac{100 \cdot \rho^{Z_k} \cdot \rho^{Z_2} \cdot r_{k2}}{\sum_{j=1}^{j=3} \rho^{Z_j} \cdot \rho^{Z_2} \cdot r_{j2}} \qquad \text{where } r_{j2} = \frac{V^{Z_j}}{V^{Z_2}} \tag{4}$$

Introducing relation (4) in (1) and re-arranging terms, the mass variation of the i^{th} component for a system conserving the total molar mass is obtained:

$$\Delta m_i = 100 \cdot \left(-C_i^R + \frac{\sum_{k=1}^{k=3} C_i^{Z_k} \cdot \rho^{Z_k} \cdot \rho^{Z_2} r_{k2}}{\sum_{k=1}^{k=3} \rho^{Z_k} \cdot \rho^{Z_2} r_{k2}} \right) \tag{5}$$

Expression (5) gives the molar variation of the i^{th} component in the product layer sequence per each of 100 moles of consumed starting rock for a metasomatic process in which the total molar mass is conserved. Relation (5) is written in such a way that $\Delta m_i > 0$ for introduction of component i into the growing wallrock. Fixing ρ^{Z_k} and $C_i^{Z_k}$ in relation (5), Δm_i is obtained as a function of r_{12} and r_{32} and, hence, it is possible to obtain a set of curves expressing Δm_i as a function of r_{12} at arbitrary values of r_{32} (Fig. 7).

The molar mass variations of non-conserved components for the amphibole-eclogite sequence have been calculated for quartz-bearing, quartz-free domains and for an average composition employing Eq. (5). The results for the range r_{12} and r_{32} ratios estimated of wallrock metasomatic layer are listed in Table 7. In spite of compositional uncertainties related to grain-scale,

Table 6 Estimated model bulk composition and mineral abundance of relicts (R)[a]

	Mean	1σ
Estimated molar mineral abundance		
Amp	0.4195	0.0043
Gar	0.0351	0.0117
Cpx	0.5454	0.0096
Estimated molar bulk composition		
Si	0.1805	0.0004
Al	0.0477	0.0006
Fe	0.0216	
Mg	0.0572	0.0009
Ca	0.0442	0.0002
Na	0.0365	0.0004
H	0.0201	0.0002
O	0.5900	
ρ	0.1590	0.0002

[a]Calculations performed assuming conservation of total molar mass, oxygen and iron with average contents of 59.00 mol% O and 2.16 mol% Fe

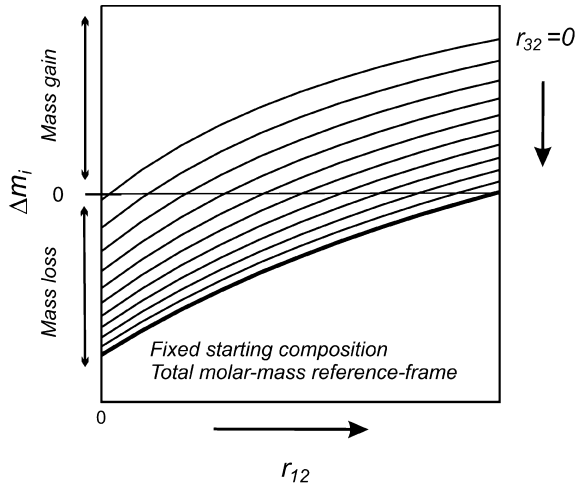

Fig. 7 Schematic relationships for molar mass variations for mobile components as a function of the volume ratio between zones 1 and 2, r_{12}. A set of *curve lines* is obtained for arbitrary V^{Z_3}/V^{Z_2} ratios, r_{32}

pore channelisation, the estimated component imbalances for the three model compositions suggest significant and systematic losses of Al and Na (a relative variation of ca. 20–30 mol%) and gains of C and H (relative variations ranging 35–60 mol%) and Mg (relative variation of ca. 10–15 mol%). Gains in Ca of up to 13 mol% could also be possible if effective wallrock compositions are close to the silicon poor model. Silicon variations are very close to the bulk composition uncertainties, suggesting that quartz rich domains could be produced by local silica segregation within each single layer.

According to these mass-balance calculations, the high-pressure veins and wallrock, amphibole-eclogite sequences from the Marun-Keu complex cannot be produced by local segregation since addition of Mg, H, C and, probably, Ca imply an external source (Fig. 8). The introduction of C and H into the wall rocks rather suggests that vein models based on local devolatilisation of the host rock cannot apply, but fluid infiltration from an external source should be required. In conclusion, mass balance analysis suggests that relatively large-scale (>metre scale) fluid circulation could be responsible for the pattern of metasomatic zones described.

Rb/Sr and Nd/Sm isotopic data in the amphibole-eclogite sequence

Rb/Sr and Sm/Nd isotopes were determined on mineral separates from different segments of sample PU-34 at

Table 7 Mass imbalances during the growth of eclogite-amphibolite sequences[a]

Model	Si mean	Si mean	Si mean	Si mean	Low Si	Low Si	Low Si	Low Si	High Si	High Si	High Si	High Si
r_{12}	0.10	0.10	0.30	0.30	0.10	0.10	0.30	0.30	0.10	0.10	0.30	0.30
r_{32}	0.30	0.70	0.30	0.70	0.30	0.70	0.30	0.70	0.30	0.70	0.30	0.70
Molar mass variation per hundred mole of protolith												
Si	−0.08	−0.28	0.12	−0.10	−0.55	−0.88	−0.30	−0.64	0.40	0.33	0.54	0.45
Al	−1.16	−1.37	−1.11	−1.31	−1.09	−1.32	−1.06	−1.27	−1.22	−1.43	−1.17	−1.36
Mg	0.76	0.78	0.55	0.61	0.87	0.88	0.65	0.70	0.65	0.68	0.45	0.52
Ca	0.17	0.26	0.27	0.33	0.38	0.56	0.45	0.59	−0.05	−0.04	0.08	0.06
Na	−0.95	−0.98	−0.76	−0.82	−0.89	−0.93	−0.70	−0.78	−1.01	−1.03	−0.81	−0.87
H	1.12	1.15	0.73	0.84	1.16	1.19	0.77	0.87	1.08	1.12	0.70	0.81
C	0.31	0.56	0.27	0.50	0.43	0.78	0.37	0.70	0.18	0.33	0.16	0.30
Relative variation, $RV_i(\%) = 100 \cdot \frac{\Delta m_i}{m_i^R}$												
Si	−0.4	−1.5	0.7	−0.5	−3.1	−4.9	−1.6	−3.5	2.2	1.8	3.0	2.5
Al	**−24.3**	**−28.8**	**−23.3**	**−27.5**	**−22.9**	**−27.7**	**−22.1**	**−26.5**	**−25.6**	**−29.9**	**−24.5**	**−28.5**
Mg	*13.3*	*13.6*	*9.6*	*10.6*	*15.2*	*15.3*	*11.3*	*12.2*	*11.3*	*11.9*	*7.9*	*9.1*
Ca	*3.8*	*5.8*	*6.0*	*7.4*	*8.7*	*12.6*	*10.2*	*13.4*	*−1.1*	*−0.9*	*1.8*	*1.3*
Na	**−26.0**	**−26.9**	**−20.7**	**−22.5**	**−24.3**	**−25.4**	**−19.3**	**−21.3**	**−27.7**	**−28.3**	**−22.2**	**−23.8**
H	*55.5*	*57.3*	*36.4*	*41.8*	*57.3*	*59.0*	*38.0*	*43.3*	*53.7*	*55.7*	*34.7*	*40.2*
C												

[a]Values calculated for the range of r_{12} and r_{32} volume ratios observed in the analysed samples

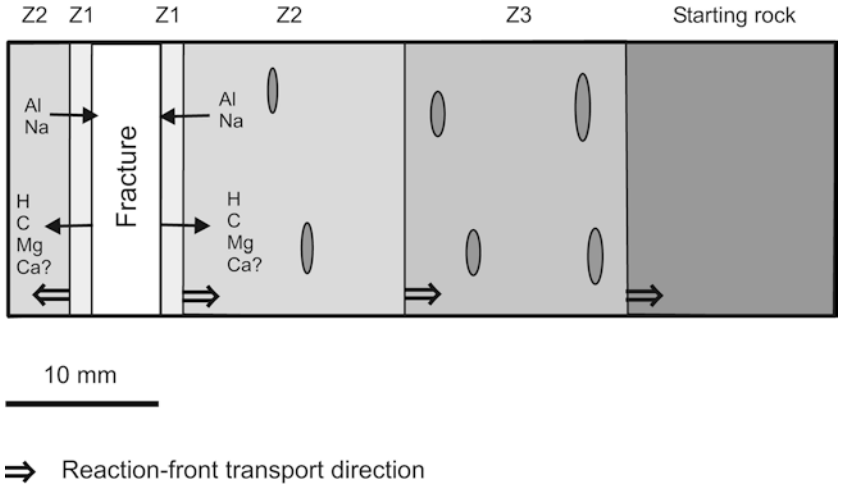

Fig. 8 Metasomatic growth model for wallrock amphibole-eclogite sequence. Mineral zones 1, 2 and 3 grow inward at expense of a starting rock with an assemblage similar to that of relicts. Al and Na are released to the fracture fluids whereas H, C and Mg (and Ca in case of silicon poor model compositions) are introduced into the wallrock. See text for discussion

the GeoForschungsZentrum Potsdam (Germany) (Tables 8 and 9; see Glodny et al. (2002) for analytical procedures). Initial isotopic compositions calculated for t = 355.5 Ma (the age of eclogite-facies metamorphism, as suggested by Glodny et al. 2003) are displayed in Fig. 9. Uncertainties on initial Sr isotopic ratios were propagated from uncertainties in Rb/Sr ratios and $^{87}Sr/^{86}Sr$ ratios, considering relative errors (at 2σ level) of, respectively, $\pm 1.5\%$ and $\pm 0.005\%$. Error propagation for initial Nd isotopic ratios was calculated considering a relative error of $\pm 0.5\%$ for Nd/Sm ratios and of $\pm 0.003\%$ for $^{143}Nd/^{144}Nd$ ratios. The analysed mineral separates show only a slight departure from perfect Nd isotopic equilibrium at the 2σ level, indicating that the initial Nd isotopic ratio of the wallrock was not (or only insignificantly) changed by fluid-rock interaction. This may suggest that both fluid and wallrock had similar initial Nd isotopic ratios or that there were negligible Nd concentrations in the fluids.

In contrast to the Nd isotopic data, initial Sr isotope ratios show significant isotopic disequilibrium at the 2σ level, with a scatter at the scale of a single mineral zone. This is consistent with the complex fluid-rock interaction history suggested by the textural observations and mass-balance calculations. Even minerals from the vein itself display significant disequilibrium. Sr isotope data for apatite from the vein suggest that the initial Sr ratio was ~0.70945 (Fig. 9). This value differs significantly from

Table 8 Rb/Sr analytical data

Sample	Material	Rb (ppm)	Sr (ppm)	$^{87}Rb/^{86}Sr$	$^{87}Sr/^{86}Sr$	$^{87}Sr/^{86}Sr$ $2\sigma_m$ (%)
PS812	34EX pheng	446	362.1	3.567	0.728172	0.0014
PS817	34 V ap	0.82	2,789	0.001	0.709456	0.0014
PS808	34 V omp	4.26	49.99	0.247	0.710433	0.0014
PS828	34Z1 omp	0.62	61.25	0.029	0.709651	0.0014
PS829	34Z2 ap	0.17	554.5	0.001	0.709522	0.0012
PS826	34Z2 omp	0.32	64.47	0.014	0.709763	0.0016
PS811	34Z2 amp	3.06	54.53	0.162	0.710313	0.0012
PS804	34Z3 omp	1.27	73.04	0.050	0.709947	0.0016
PS807	34Z3 carb	1.07	960.5	0.003	0.709255	0.0014

Errors are reported at the 2σ level. An uncertainty of $\pm 1.5\%$ has to be assigned to Rb/Sr ratios

Table 9 Sm/Nd analytical data

Sample	Material	Sm (ppm)	Nd (ppm)	$^{147}Sm/^{144}Nd$	$^{143}Nd/^{144}Nd$	$^{143}Nd/^{144}Nd$ $2\sigma_m$ (%)
PS817	34 V ap	277.4	1,033	0.1623	0.512135	0.0016
PS808	34 V omp	3.883	19.67	0.1193	0.512020	0.0015
PS822	34 V gar	3.864	7.896	0.2959	0.512453	0.0015
PS828	34Z1 omp	3.280	10.70	0.1854	0.512175	0.0015
PS826	34Z2 omp	2.552	6.254	0.2467	0.512353	0.0014
PS811	34Z2 amp	3.112	7.193	0.2616	0.512389	0.0015
PS804	34Z3 omp	2.727	7.991	0.2063	0.512267	0.0013
PS807	34Z3 carb	65.54	444.04	0.0892	0.511990	0.0012

Errors are reported at the 2σ level. An uncertainty of $\pm 0.5\%$ has to be assigned to Sm/Nd ratios

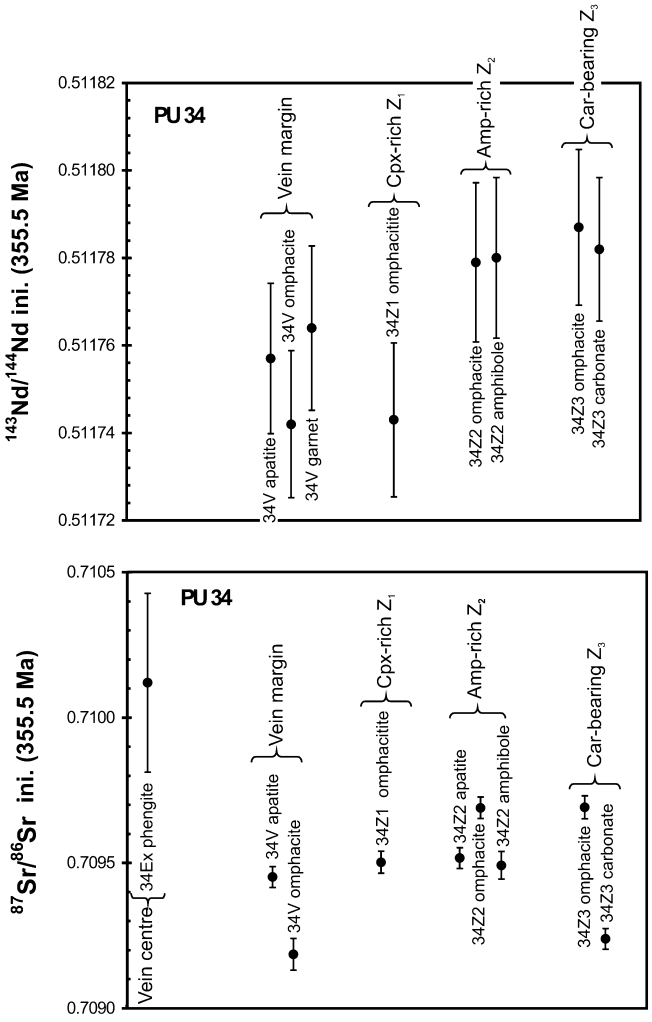

Fig. 9 Initial Nd and Sr isotope ratios for minerals from vein precipitates and wallrock assemblages from sample PU-34. Values were calculated at 355.5 Ma, which is the best age estimate for the high-P fluid-rock interaction processes in the Marun-Keu complex (Glodny et al. 2003). Assemblages qualitatively displayed as a function of the distance to the centre of the vein. *Error bars* at 2σ level

the initial Sr ratios inferred from the Rb/Sr isotopic data for phengite (~0.71012) and omphacite (~0.70919) from the vein (Fig. 9). These data suggest that the Sr isotopic composition of the fluids varied during mineral growth, which is consistent with >metre scale circulation of fluids during the growth of the wallrock sequences. This does not necessarily preclude short-range circulation, as seen in different localities within the Marun-Keu complex (Glodny et al. 2003).

Temperature estimates for vein precipitates and wallrock assemblages: time scales for fluid circulation in the Marun-Keu complex

Much scatter of $Fe^{2+}/(Fe^{2+}+Mg)$ ratios is seen for garnet, clinopyroxene and amphibole from the different mineral zones in the amphibole-eclogite blocks, which suggest temperatures changed during their growth. Temperatures were calculated employing various calibrations of the garnet-clinopyroxene thermometer (Ellis and Green 1979; Krogh 1988; Ai 1994). In addition, temperatures were also computed by non-linear mineral-equilibrium calculations (as described in Molina and Poli 2000), which are based on free energy minimisation algorithms (e.g. Connolly 1990). These calculations were performed using the thermodynamic database of Holland and Powell (1998) with solution models for garnet from Berman (1990) and for clinopyroxene from Holland (1990).

Differences in calculated temperatures among these calibrations are large, but consistent temperature variations across the mineral zones are obtained with each method (Table 10). There is no correlation between computed temperatures and grossular content of garnet (Table 10), indicating that compositional dependences of Fe/Mg partitioning between garnet and clinopyroxene were properly corrected by the solution models. Therefore, although temperature estimates might not be accurate, the relative temperature variations are well constrained. Temperatures computed by non-linear equilibrium calculations are close to those obtained with the calibration of Krogh (1988) and will be used in the discussion that follows.

Clinopyroxene inclusions in garnet from **R** yield the lowest T estimates, 408–434 °C (Table 10). The highest T values are obtained for garnet-clinopyroxene pairs from vein assemblages (526 °C in sample J-10, 668 °C in PU-34). T estimates for garnet-clinopyroxene pairs from mineral Z_1 are slightly higher than those for core compositions from **R**, with values of 435 to 490 °C in J-10 (Fig. 10a) and 490 to 575 °C in PU-34 (Fig. 10b). T estimates for rim assemblages from **R** show a bimodal distribution, with one population yielding ~400 to 420 °C (similar to cores) and another one that ranges from 460 to 530 °C (like from Z_1).

Fe/Mg partition coefficients between amphibole and garnet, $Kd_{Fe/Mg}^{Amp/Gar}$ display the highest values in amphibole-garnet pairs at resorption rims, and the lowest in amphibole inclusions in garnet from relicts (Table 11). On average, temperatures using the garnet-amphibole thermometer of Graham and Powell (1984) for the various assemblages are consistent with the relative temperature variations detected by garnet-clinopyroxene thermometry (Table 11) also suggesting a significant temperature increase during garnet resorption.

Therefore, a prograde thermal history is recorded in the metasomatic blocks from the Marun-Keu complex, with the minimum temperatures (408–434 °C) in omphacite-garnet-amphibole patches (**R**) and maximum temperatures (526–668 °C) in the vein precipitates. The observed temperature differences (ca. 150–200 °C) are unusual for similar assemblages over such a short distance and significantly high when compared to single medium-T eclogite-facies terrains reported in the literature (e.g. Cuthbert and Carswell 1990; O'Brien et al.

Table 10 Garnet-clinopyroxene thermometry (°C)[a, b]

J-10										
Zone	V. C.	V. C.	V. M.	V. M.	V. M.	V. M.	V. M.	V. M.	V. M.	Z1
Texture	Rim	Rim	Rim	Rim	Rim	Rim	Rim	Rim	Rim	Rim
$Kd^{Cpx/Gar}_{Fe/Mg}$	0.068	0.083	0.063	0.052	0.055	0.058	0.056	0.078	0.086	0.062
Gro	0.227	0.213	0.155	0.193	0.186	0.167	0.216	0.151	0.214	0.158
E. C.	485 ± 44	526 ± 58	455 ± 43	427 ± 44	437 ± 44	443 ± 44	450 ± 43	493 ± 58	534 ± 57	452 ± 42
T (E&G, 79)	574	603	515	507	512	509	535	548	612	514
T (K, 88)	563	592	475	480	484	473	518	508	602	474
T (A, 94)	471	507	412	401	404	404	437	436	498	403
Zone	Z1	Z1	Z1	R	R	R	R	R	R	R
Texture	rim	rim	rim	rim	core	core	rim	core	rim	rim
$Kd^{Cpx/Gar}_{Fe/Mg}$	0.055	0.076	0.06	0.046	0.053	0.048	0.048	0.04	0.067	0.092
Gro	0.171	0.152	0.146	0.158	0.167	0.167	0.175	0.151	0.153	0.138
E. C.	434 ± 44	490 ± 44	440 ± 43	399 ± 41	425 ± 43	408 ± 42	408 ± 41	419 ± 43	461 ± 44	462 ± 44
T (E&G, 79)	502	545	501	467	495	479	482	442	522	570
T (K, 88)	468	505	456	425	458	441	448	396	481	524
T (A, 94)	390	429	373	347	372	355	358	325	404	442
PU-34										
Zone	V. M.	V. M.	V. M.	V. M.	Z1	Z1	Z1	Z1	Z1	R
Texture	Rim	Rim	Rim	Rim	Rim	Rim	Rim	Rim	Rim	Rim
$Kd^{Cpx/Gar}_{Fe/Mg}$	0.149	0.134	0.125	0.097	0.076	0.091	0.092	0.08	0.107	0.054
Gro	0.163	0.166	0.15	0.135	0.147	0.144	0.167	0.177	0.173	0.146
E. C.	668 ± 61	637 ± 62	614 ± 61	537 ± 55	487 ± 45	526 ± 57	539 ± 56	509 ± 48	575 ± 57	421 ± 42
T (E&G, 79)	698	676	647	581	541	574	593	573	627	483
T (K, 88)	680	656	615	535	498	533	564	547	604	436
T (A, 94)	583	563	536	455	425	450	481	472	521	363
Zone	R	R	R	R	R					
Texture	Core	Rim	Rim	Rim	Rim					
$Kd^{Cpx/Gar}_{Fe/Mg}$	0.058	0.077	0.077	0.092	0.076					
Gro	0.151	0.128	0.162	0.139	0.152					
E. C.	434 ± 43	482 ± 44	496 ± 44	530 ± 57	490 ± 48					
T (E&G, 79)	497	531	556	572	546					
T (K, 88)	454	478	522	528	506					
T (A, 94)	377	403	431	459	421					

[a]Calculations performed at a nominal pressure of 15 kbar
[b]*E.C.*: equilibrium calculations (see text); *E&G* Ellis and Green (1979); *K* Krogh (1988); *A* Ai (1994)

1990) and further discussion is required. These temperature variations are unlikely to represent an instantaneous thermal boundary layer between the vein and the relict eclogite unless hot, disequilibrium fluids were emplaced extremely fast. Instead, this fossil thermal gradient testifies to a continuous fluid-rock interaction within a terrain that is undergoing thermal relaxation.

Eclogite-facies metamorphism in the Urals occurred during east-directed subduction of oceanic lithosphere (e.g. Bea et al. 1997; Fershtater et al. 1997; Montero et al. 2000), followed by arc-continent collision (Chemenda et al. 1997). Accordingly, it is likely that eclogite-facies metamorphism of the Marun-Keu complex affected rocks of the East European margin when it collided with an island arc complex. The relatively high temperatures achieved in the Marun-Keu complex contrast with other high-P complexes of the Urals, that are characterized by glaucophane-bearing eclogites (e.g. Maksyutov complex, Sobolev et al. (1986); see also Molina et al. (2002) and references therein). Further evidence for warm thermal regimes during Uralian subduction is seen in subduction-related granitoids of adakite affinity in the Verkhisetsk batholith (Central Urals), which are interpreted to reflect melting of the oceanic subducted crust (Bea et al. 1997).

Mechanisms for the relatively high temperatures of the Marun-Keu complex are suggested by the contrasting temperature estimates for vein precipitates and wallrock assemblages. $P–T_{max}$ conditions for the eclogite-facies bodies unaffected by veining in the Marun-Keu complex are 14–17 kbar and 600–650 °C (Molina et al. 2002). Therefore, since maximum T estimates for vein precipitates are close to peak T conditions in the overall terrain, the last veins should have formed at depths equivalent to ~14–17 kbar (Fig. 11). As pressure estimates for early stages of metasomatism are barely defined, two scenarios are possible: (1) onset of the fluid-rock interaction during an earlier subduction stage (path 1 in Fig. 11); or (2) fluid-rock interaction process entirely during a decompression path (2 in Fig. 11). Whatever the path, cessation of fluid-rock interaction at peak T is likely a consequence of the P–T dependence of mineral solubilities in aqueous fluids. Decompressional retrograde paths present dramatic consequences for the stability of the fluid circulation as precipitation of the material dissolved in the vein fluids is expected, as a

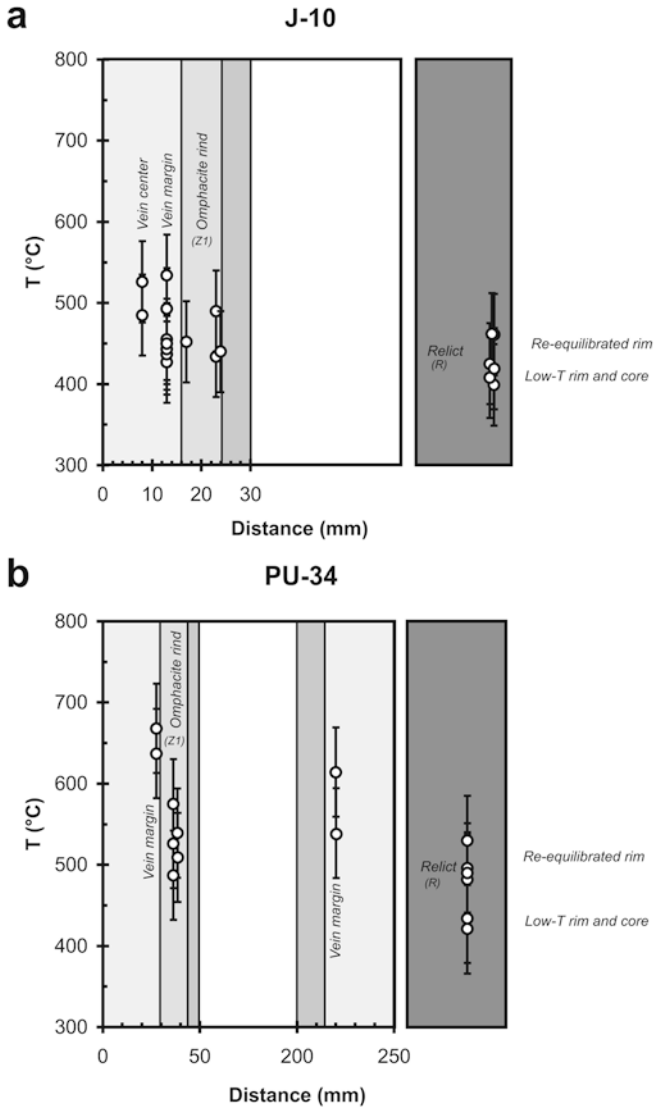

Fig. 10 Temperature estimations in vein and wallrock assemblages from samples J-10 and PU-34. **a** Temperature estimates in J-10 vs. distance to the vein. **b** Temperature estimates in PU-34 vs. distance to the vein. Unspecified location for temperature estimates from relicts. Calculations performed by non-linear equilibrium methods

result of decreasing silica solubility with decreasing P and T (e.g. Newton and Manning 2000), leading to a reduction of permeability and, hence, choking of fluid circulation.

Some time constraints for the growth of the metasomatic sequence and for the material precipitation in the veins can be obtained by comparing textural relationships to mechanical models predicting the propagation of cracks. The last vein mineral crystallized when the growth of the metasomatic zones ceased. Because veins are parallel to the boundaries of the blocks and to the wallrock metasomatic layers suggests that both the vein precipitation and growth of the metasomatic sequence occurred during a single fluid infiltration event. Otherwise, we would expect some crosscutting between the high temperature veins and the metasomatic layers. The stability of a crack is mostly controlled by (1) fluid pressure in the crack and hydraulic gradients, (2) the ability of crack to close once fluid pressure is reduced, and (3) vein precipitation, which may eventually fill the whole open fracture (Oliver and Bons 2001). Mechanical models for crack propagation predict that fractures can propagate without introducing more fluid when the effective tensile stress at the upper tip of the crack exceeds the fracture toughness of the wallrock as it closes simultaneously at its lower end (e.g. Secor and Pollard 1975; Oliver and Bons 2001). On the basis of mechanical and geochemical constraints, estimates of the time scales for the duration of fluid-rock interaction processes in crustal terrains are in the order of 10^4-10^6 years (Bickle and Baker 1990a, 1990b; Jenkin et al. 1992; Young and Rumble 1993; van Haren et al. 1996; Connolly 1997; Graham et al. 1998). Therefore, the temperature increase recorded during the growth of the wallrock sequence and the precipitation of the vein precipitates should imply heating rates of ≥100 °C/Ma.

Huerta et al. (1999) performed two-dimensional thermal models for collisional metamorphism including the contribution of radiogenic heat production of the crust. According to such models, discontinuous and episodic accretion of material from the down-going plate to the over-riding plate leads to higher heating rates (> 10 °C/Ma) than continuous accretion. However, the heating rates suggested for the deep fluid-rock interaction process of the Marun-Keu complex cannot be explained under the various conditions modelled by Huerta et al. (1999), which should require time periods of ca. 3–5 Ma (Fig. 11). On the other hand, thermal models for fluid circulation (e.g. Brady 1988; Connolly 1997) establish that heat advection by large-scale circulation of fluids with high fluxes and strong channelisation component can effectively affect the thermal regime, predicting temperature variations > 50 °C over short time periods (< 1 Ma) for fluid fluxes of ca. 10^{-8}–10^{-7} kg $m^{-2}s^{-1}$ (Connolly 1997).

As a conclusion, significant contribution of heat transported by the fracture fluid may provide an explanation for the high-heating rates inferred for the fluid-rock interaction process, implying fluid circulation over a large scale, which is consistent with the open-behaviour suggested by mass-balance calculations and by isotopic disequilibria.

Concluding remarks

The Marun-Keu complex presents high-pressure vein systems with development of wallrock amphibole-eclogite sequences characterised by: (1) band organization roughly parallel to the veins; (2) systematic compositional variations of clinopyroxene and amphibole as a function of the distance to the vein; (3) significant bulk chemistry variations through the various mineral layers

Table 11 Garnet-amphibole thermometry (°C)[a]

J-10														
Zone	V.C.	V.C.	V.M.	V.M.	V.M.	V.M.	V.M.	V.M.	V.M.	V.M.	V.M.	V.M.	V.M.	V.M.
Texture	Rim	Rim	Rim	Rim	Rim	Rim	Inc	Rim	Rim	Rim	Rim	Rim	Rim	Rim
$Kd^{Amp/Gar}_{Fe/Mg}$	0.198	0.249	0.172	0.187	0.236	0.224	0.266	0.181	0.191	0.214	0.215	0.224	0.24	0.275
Gro	0.213	0.22	0.167	0.155	0.151	0.18	0.214	0.184	0.178	0.176	0.176	0.118	0.138	0.118
T (G&P, 84)	611	671	546	553	599	611	682	569	576	598	599	560	591	606
Zone	R	R	R	R	R	R	R	R	R	R	R	R	R	R
Texture	Inc	Res	Inc	Res	Res	Res	Res	Rim	Rim	Res	Res	Rim	Rim	Rim
$Kd^{Amp/Gar}_{Fe/Mg}$	0.142	0.237	0.126	0.264	0.246	0.17	0.212	0.147	0.129	0.174	0.205	0.147	0.136	0.145
Gro	0.154	0.159	0.154	0.157	0.142	0.167	0.167	0.144	0.122	0.151	0.152	0.158	0.16	0.16
T (G&P, 84)	500	606	480	630	601	543	589	499	460	535	570	510	498	509
PU-34														
Zone	V.C.	V.C.	V.C.	V.C.	V.C.	V.M.	V.M.	V.M.	V.M.	V.M.	Z1	Z1	Z1	Z1
Texture	Inc	Rim	Inc	Rim	Inc	Rim	Rim	Rim	Rim	Rim	Rim	Rim	Rim	Rim
$Kd^{Amp/Gar}_{Fe/Mg}$	0.171	0.248	0.286	0.309	0.174	0.211	0.247	0.168	0.162	0.188	0.174	0.167	0.176	0.186
Gro	0.171	0.142	0.173	0.161	0.129	0.166	0.16	0.114	0.16	0.126	0.147	0.173	0.173	0.165
T (G&P, 84)	548	602	664	673	519	587	617	500	529	530	533	544	555	560
Zone	Z1	R	R	R	R	R	R	R	R	R	R	R	R	R
Texture	Rim	Res	Res	Res	Res	Res	Res	Inc	Inc	Inc	Res	Res	Rim	Rim
$Kd^{Amp/Gar}_{Fe/Mg}$	0.183	0.262	0.309	0.267	0.32	0.225	0.328	0.188	0.144	0.166	0.257	0.225	0.153	0.192
Gro	0.173	0.151	0.154	0.139	0.157	0.161	0.163	0.145	0.146	0.146	0.17	0.196	0.171	0.115
T (G&P, 84)	562	623	667	617	680	597	691	546	497	522	635	626	527	526

[a]*G&P* Graham and Powell (1984)

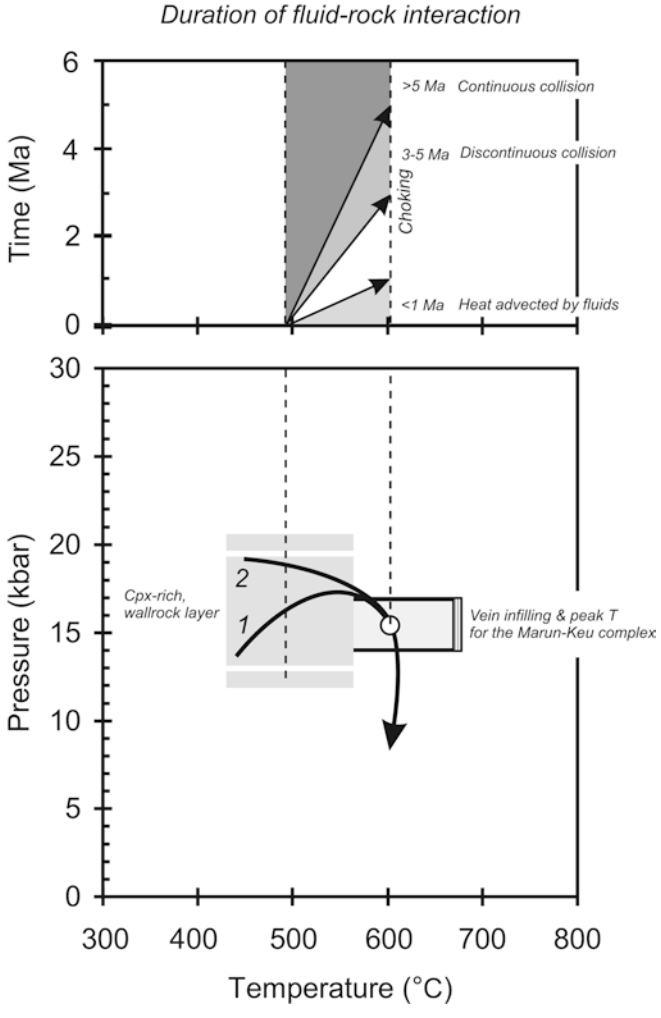

and net mass-exchange between the wallrock and the vein fluids; (4) Rb/Sr disequilibria at the scale of the vein-wallrock system; and (5) significant temperature increase during the growth of the mineral sequence and the vein precipitation.

This evidence indicates that the growth of the amphibole-eclogite sequences was caused by a fracture-related metasomatism due to the circulation of hot disequilibrium fluids over > metre (and possibly kilometre) scales during the eclogite-facies metamorphism.

The Marun-Keu complex offers a new perspective on eclogite-facies metasomatic processes and provides evidence for open system behaviour during high-P metamorphism with large scale-transport of both mass and heat.

Acknowledgements We thank Muriel Erambert and Jane H. Scarrow for their constructive comments. The help of Jane H. Scarrow in improving the English is also gratefully acknowledged. We are indebted to V. Koroteev, V.I. Lennykh and V. Pease for excellent guidance and company in the field. Field work in the Polar Urals was made possible through a grant from the Nansen Foundation to H. Austrheim. We are indebted to R. Abart and S. Sorensen for constructive reviews. This work was funded by projects ERB-FMRXCT96-0009 (TMR-URO Programme from the European Commission), MIUR-COFIN 2003 (Italian MURST) and BTE 2002-04618-CO2-01 (Spanish DGICYT), and by Fellowship of the University of Milan to J-F. M.

◄

Fig. 11 P–T conditions for the fluid-rock interaction process in the Marun-Keu complex constrained from temperature estimates in wallrock-clinopyroxene-rich assemblages and vein precipitates. Metamorphic conditions at temperature peak as estimated by Molina et al. (2002). See text for discussion

Appendix

The Gresens-Grant equations

According to Grant (1986), the initial and final concentrations of the i^{th} component, respectively, C_i^o and C_i^F are related by the following expression:

$$C_i^F = \frac{m^o}{m^F} \cdot \left(C_i^o + \Delta C_i\right) \tag{A1}$$

where m^o and m^F are the equivalent masses prior to and after the transformation and ΔC_i is the gain or loss of mass of the i^{th} component, Δm_i, divided by m^o:

$$\Delta C_i = \frac{\Delta m_i}{m^o} \tag{A2}$$

Since ΔC_i is null for those components which remain immobile during the metasomatic process, from expression (A1) the following relation is derived for immobile components:

$$\frac{m^o}{m^F} = \frac{C_i^F}{C_i^o} \tag{A3}$$

Relation (A3) implies that C_i^F and C_i^o values for immobile components must define a straight line through the origin giving by the equation:

$$C^F = \frac{m^o}{m^F} \cdot C^o \tag{A4}$$

which was named isocon by Grant (1986).

According to relation (A3), the isocon equation becomes:

$$C^F = \frac{C_n^F}{C_n^o} \cdot C^o$$

for a process conserving the n^{th} component;

$$C^F = C^o$$

for constant mass; and

$$C^F = \frac{\rho^o}{\rho^F} \cdot C^o$$

for constant volume (where ρ is the rock density).

Dividing relation (A1) by C_i^o and re-arranging terms, we obtain:

$$C_i^F = C_i^o \cdot \frac{m^o}{m^F} \cdot \left(1 + \frac{\Delta C_i}{C_i^o}\right) \tag{A5}$$

which indicates that all components experiencing the same relative variation must lie on a line through the origin. It is important to note that $\Delta C / C_i^o$ is the relative mass variation of the i^{th} component referred to the masses of that component prior to the metasomatic transformation:

$$\frac{\Delta C_i}{C_i^o} = \frac{\Delta m_i}{m_i^o} \tag{A6}$$

References

Ague JJ (1994a) Mass transfer during Barrovian metamorphism of pelites, south-central Connecticut, I: evidence for composition and volume change. Am J Sci 294:989–1057

Ague JJ (1994b) Mass transfer during Barrovian metamorphism of pelites, south-central Connecticut, II: channelized fluid flow and the growth of staurolite and kyanite. Am J Sci 194:1061–1134

Ai Y (1994) A revision of the garnet-clinopyroxene Fe^{2+}-Mg exchange geothermometer. Contrib Mineral Petrol 115:467–473

Altaner SP, Ylagan RF, Savin SM, Aronson JL, Belkin HE, Pozzuoli A (2003) Geothermometry, geochronology, and mass transfer associated with hydrothermal alteration of a rhyolitic hyaloclastite form Ponza Island, Italy. Geochim Cosmochim Acta 67:275–288

Anderson GM (1976) Error propagation by the Monte Carlo method in geochemical calculations. Geochim Cosmochim Acta 40:1533–1538

Ashworth JR, Birdi JJ (1990) Diffusion modelling of corona around olivine in an open system. Geochim Cosmochim Acta 54:2389–2401

Ashworth JR, Sheplev VS (1997) Diffusion modelling of metamorphic layered coronas with stability criterion and consideration of affinity. Geochim Cosmochim Acta 61:3671–3689

Austrheim H (1987) Eclogitization of the lower crustal granulites by fluid migration through shear zones. Earth Planet Sci Lett 81:221–232

Austrheim H (1998) Influence of fluids and deformation on metamorphism of the deep crust and consequences for the geodynamics of collision zones. In: Hacker BR, Liou JG (eds) Geodynamics and geochemistry of ultrahigh-P rocks. Kluwer Academic, Dordrecht, pp 297–323

Austrheim H, Engvik AK (1997) Fluid transport, deformation and metamorphism at depth in a collision zone. In: Jamtveit B, Yardley BWD (eds) Fluid flow and transport in rocks. Chapman & Hall, London, pp 123–135

Austrheim H, Erambert M, Engvik AK (1997) Processing of crust in the root of the Caledonian continental collision zone: the role of eclogitization. Tectonophysics 273:129–153

Barnicoat AC, Cartwright I (1995) Focused fluid flow during subduction: oxygen isotope data from high-pressure ophiolites of the western Alps. Earth Planet Sci Lett 132:53–61

Baumgartner LP, Olsen SN (1995) A least-square approach to mass transport calculation using the isocon method. Econ Geol 90:1261–1270

Bea F, Fershtater G, Montero P, Smirnov V, Zin'kova E (1997) Generation and evolution of subduction-related batholiths from the central Urals: constraints on the P–T evolution history of the Uralian orogen. Tectonophysics 276:103–116

Bebout G, Barton MD (1993) Metasomatism during subduction: products and possible paths in the Catalina Schist, California. Chem Geol 108:61–92

Berman RG (1990) Mixing properties of Ca-Mg-Fe-Mn garnets. Am Mineral 75:328–344

Bickle MJ, Baker J (1990a) Advective-diffusive transport of isotope fronts: an example from Naxos, Greece. Earth Planet Sci Lett 97:78–93

Bickle, MJ, Baker J (1990b) Migration of reaction and isotopic fronts in infiltration zones: assessment of fluid flux in metamorphic terrains. Earth Planet Sci Lett 98:1-13

Bickle MJ, McKenzie D (1987) The transport of heat and matter by fluids during metamorphism. Contrib Mineral Petrol 95:384–392

Brady JB (1975) Reference frames and diffusion coefficients. Am J Sci 275:954–983

Brady JB (1988) The role of volatiles in the thermal history of metamorphic terranes. J Petrol 29:1187–1213
Cail TL, Cline JS (2001) Alteration associated with gold deposition at the Getchell Carlin-type gold deposit, North-Central Nevada. Econ Geol 96:1343–1359
Cesare B (1994) Synmetamorphic veining: origin of andalusite-bearing veins in the Vedrette di Ries contact aureole, eastern Alps, Italy. J Metamorph Geol 12:643–653
Chamberlain CP, Rumble D (1988) Thermal anomalies in a regional metamorphic terrane: an isotopic study of the role of fluids. J Petrol 29:1215–1232
Chemenda A, Matte P, Sokolov V (1997) A model of Paleozoic obduction and exhumation of high-pressure/low-temperature rocks in the southern Urals. Tectonophysics 276:217–227
Connolly JAD (1990) Multivariable phase diagrams: an algorithm based on generalized thermodynamics. Am J Sci 290:666–718
Connolly JAD (1997) Mid-crustal focused fluid movement: thermal consequences and silica transport. In: Jamtveit B, Yardley BWD (eds) Fluid flow and transport in rocks. Chapman & Hall, London, pp 235–250
Cuthbert SJ, Carswell DA (1990) Formation and exhumation of medium-temperature eclogites in the Scandinavian Caledonides. In: Carswell DA (ed) Eclogite-facies rocks. Blackie, Glasgow, pp 180–203
Dobretsov NL, Sobolev NV (1984) Glaucophane schists and eclogites in folded systems from Northern Asia. Ofioliti 9:401–424
Ellis DJ, Green DH (1979) An experimental study of the effect of Ca upon garnet-clinopyroxene Fe-Mg exchange equilibria. Contrib Mineral Petrol 71:13–22
Fershtater GB, Montero P, Borodina NS, Pushkarev EV, Smirnov VN, Bea F (1997) Uralian magmatism: an overview. Tectonophysics 276:87–102
Getty SR, Selverstone J (1994) Stable isotopic and trace-element evidence for restricted fluid migration in 2 GPa eclogite. J Metamorph Geol 12:747–760
Glodny J, Austrheim H, Molina JF, Rusin A, Seward D (2003) Rb/Sr record of fluid-rock interaction in eclogites: the Marun-Keu complex, Polar Urals, Russia. Geochim Cosmochim Acta 67:4353–4371
Glodny J, Bingen B, Austrheim H, Molina JF, Rusin A (2002) Precise eclogitization ages deduced from Sr/Rb mineral systematics: the Maksyutov complex, Southern Urals, Russia. Geochim Cosmochim Acta 66:1221–1235
Godard G, Martin S (2000) Petrogenesis of kelyphites in garnet peridotites: case study from the Ulten zone, Italian Alps. J Geodyn 30:117–145
Graham CM, Powell R (1984) A garnet-hornblende geothermometer: calibration, testing, and application to the Pelona Schist, Southern California. J Metamorph Geol 2:13–31
Graham CM, Valley JW, Eiler JM, Wada H (1998) Timescales and mechanisms of fluid infiltration in a marble: an ion microprobe study. Contrib Mineral Petrol 132:371–389
Grant JA (1986) The isocon diagram: a simple solution to Gresens' equation for metasomatic alteration. Econ Geol 81:1976–1982
Gresens RL (1967) Composition-volume relationships of metasomatism. Chem Geol 2:47–65
Holland TJB (1990) Activities of components in omphacitic solid solution: an application of Landau theory to mixtures. Contrib Mineral Petrol 105:446–453
Holland TJB, Powell R (1998) An internally consistent thermodynamic data set for phases of petrological interest. J Metamorph Geol 16:309–343
Huerta AD, Royden LH, Hodges KV (1999) The effect of accretion, erosion and radiogenic heat on the metamorphic evolution of collisional orogens. J. Metamorph Geol 17:349–366
Jamtveit B, Austrheim H, Malthe-Sorenssen A (2000) Accelerated hydration of the Earth's deep crust induced by stress perturbations. Nature 408:75–78
Jamtveit B, Bucher-Nurminen K, Austrheim H (1990) Fluid controlled eclogitization of granulites in deep crust shear zones, Bergen Arcs, Western Norway. Contrib Mineral Petrol 104:184–193
Jenkin GRT, Fallick AE, Leake BE (1992) A stable isotope study of retrograde in SW Connemara, Ireland. Contrib Mineral Petrol 110:269–288
Kerrick DM, Connolly JAD (2001) Metamorphic devolatilization of subducted mid-ocean ridge metabasalts: implications for seismicity, arc magmatism and volatile recycling. Earth Planet Sci Letter 189:19–29
Krogh EJ (1988) The garnet-clinopyroxene Fe-Mg geothermometer—a reinterpretation of existing experimental data. Contrib Mineral Petrol 99:44–48
Lennykh VI, Valizer P, Schulte BA (1997) Eclogites and blueschists of the Urals: evolution and geodynamics. Terra Nova 9:17
Liou JG, Zhang RY, Ernst WG, Rumble III D, Maruyama S et al (1998) High-pressure minerals from deeply subducted metamorphic rocks. In: Hemley RJ (ed) Ultrahigh-pressure mineralogy: physics and chemistry of the Earth's deep interior. Rev Min 37:33–96
Markl G, Abart R, Vennemann T, Sommer H (2003) Mid-crustal metasomatic reaction veins in a spinel peridotite. J Petrol 44:1097–1120
Molina JF, Austrheim A, Glodny J, Rusin A (2002) The eclogites of the Marun-Keu complex, Polar Urals (Russia): fluid control on reaction kinetics and metasomatism during high-P metamorphism. Lithos 61:55–78
Molina JF, Poli S (2000) Carbonate stability and fluid composition in subducted oceanic crust: an experimental study on H_2O-CO_2 -bearing basalts. Earth Planet Sci Lett 176:295–310
Montero P, Bea F, Gerdes A, Fershtater G, Zin'kova E, Borodina N, Osipova T, Smirnov V (2000) Single-zircon evaporation ages and Rb-Sr dating of four major Variscan batholiths of the Urals. A perspective on the timing of deformation and granite generation. Tectonophysics 317:93–108
Nelson BM (1995) Fluid flow in subduction zones: evidence from Nd- and Sr-isotope variations in metabasalts of the Franciscan complex, California. Contrib Mineral Petrol 119:247–262
Newton RC, Manning CE (2000) Quartz solubility in H_2O-NaCl and H_2O-CO_2 solutions at deep crust-upper mantle pressures and temperatures: 2–15 kbar and 500–900 °C. Geochim Cosmochim Acta 64:2993–3005
Nijland TG, Touret JLR (2001) Replacement of graphic pegmatite by graphic albite-actinolite-clinopyroxene intergrowths (Mjavatn, southern Norway). Eur J Mineral 13:41–50
O'Brien PJ, Carswell DA, Gebauer D (1990) Eclogite formation and distribution in the Variscides. In: Carswell DA (ed) Eclogite-facies rocks. Blackie, Glasgow, pp 204–224
Oliver NHS (1996) Review and classification of structural controls on fluid flow during regional metamorphism. J Metamorph Geol 14:477–492
Oliver NHS, Bons PD (2001) Mechanisms of fluid flow and fluid-rock interaction in fossil metamorphic hydrothermal systems inferred from vein-wallrock patterns, geometry and microstructures. Geofluids 1:137–162
Pawley AR, Holloway JR (1993) Water sources for subduction zone volcanism: new experimental constrains. Science 260:664–667
Philippot P (1993) Fluid-melt-rock interaction in mafic eclogites and coesite-bearing metasediments: constraints on volatile recycling during subduction. Chem Geol 108:93–112
Philippot P, Chevallier P, Chopin C, Dubessy J (1995) Fluid composition and evolution in coesite-bearing rocks (Dora-Maira massif, western Alps): implications for element recycling during subduction. Contrib Mineral Petrol 121:29–44
Philippot P, Scambelluri M (1995) The composition and behaviour of fluids in high-pressure rocks from the Alps: a review. In: Lombardo B (ed) Studies on metamorphic rocks and minerals of the western Alps. A volume in Memory of Ugo Pognante. Boll Museo Reg Sci Nat, Torino 13:76–101
Poli S, Schmidt MW (2002) Petrology of subducted slabs. Ann Rev Earth Planet Sci 30:207–235
Savelieva GN, Nesbitt RW (1996) A synthesis of the stratigraphic and tectonic setting of the Uralian ophiolites. J Geol Soc Lond 153:525–537

Scambelluri M, Pennacchioni G, Philippot P (1998) Salt-rich aqueous fluids formed during eclogitization of metabasites in the Alpine continental crust (Austroalpine Mt. Emilius unit, Italian western Alps). Lithos 43:151–167

Scambelluri M, Philippot P (2001) Deep fluids in subduction zones. Lithos 55:213–227

Scarrow JH, Pease V, Fleutelot C, Dushin V (2001) The late Neoproterozoic Enganepe ophiolite, Polar Urals, Russia: an extension of the Cadomian arc? Precambrian Res 110:255–275

Schmidt MW, Poli S (1998) Experimentally based water budgets for dehydrating slabs and consequences for arc magma generation. Earth Planet Sci Lett 163:361–379

Schmidt MW, Poli S (2003) Generation of mobile components during oceanic crust subduction. In: Holland HD, Turekian KK (eds) Treatise on geochemistry, vol 3: The crust (Rudnick RL, ed). Chap 21. Elsevier, Amsterdam

Secor DT, Pollard DD (1975) On the stability of open hydraulic fractures in the Earth's crust. Geophys Res Lett 2:510–513

Selverstone J, Franz G, Thomas S, Getty S (1992) Fluid variability in 2-GPa eclogites as indicator of fluid behaviour during subduction. Contrib Mineral Petrol 112:341–357

Selverstone J, Hyatt J (2003) Chemical and physical responses to deformation in micaceous quartzites from Tauern Window, Eastern Alps, J Metamorph Geol 21:335–345

Sobolev NV, Dobretsov NL, Bakirov AB, Shatsky VS (1986) Eclogites from various types of metamorphic complexes in the USSR and problems of their origin. In: Evans BW, Brown EH (eds) Blueschists and eclogites. Geol Soc Am Mem 164:349–363

Sorensen SS, Grossman JN (1989) Enrichment of trace elements in garnet amphibolites from paleo-subduction zone: Catalina Schist, southern California. Geochim Cosmochim Acta 53:3155–3177

Thompson AB (1975) Calc-silicate diffusion zones between marble and pelitic schist. J Petrol 16:314–346

Thompson AB (1997) Flow and focusing of metamorphic fluids. In: Jamtveit B, Yardley BWD (eds) Fluid flow and transport in rocks. Chapman & Hall, London, pp 297–314

Thompson JB Jr (1959) Local equilibrium in metasomatic processes. In: Abelson PM (ed) Research in geochemistry. Wiley, New York, pp 427–457

Udovkina NG (1971) Eclogites of Polar Urals (in Russian). Nauka, Moscow

Van Haren JLM, Ague JJ, Rye DM (1996) Oxygen isotope record of fluid infiltration and mass transfer during regional metamorphism of pelitic schist, Connecticut, USA. Geochim Cosmochim Acta 60:3487–3504

Wark AD, Watson EB (2002) Grain-scale channelization of pores due to gradients in temperature or composition of intergranular fluid or melt. J Geophys Res 107B:1–15

Widmer T, Thompson AB (2001) Local origin of high pressure vein material in eclogite facies rocks of the Zermatt-Saas Zone, Switzerland. Am J Sci 301:627–656

Yardley BWD, Bottrell, SH (1992) Silica mobility and fluid movement during metamorphism of the Connemara schists, Ireland. J Metamorph Geol 10:453–464

Yaxley GM, Green DH (1994) Experimental demonstration of refractory carbonate-bearing eclogite and siliceous melt in the subduction regime. Earth Planet Sci Lett 128:313–325

Yonkee WA, Parry WT, Bruhn RL (2003) Relations between progressive deformation and fluid-rock interaction during shear-zone growth in a basement-cored thrust sheet, Servier orogenic belt, Utha. Am J Sci 303:1–59

Young ED, Rumble D (1993) The origin of correlated variations in in-situ $^{18}O/^{16}O$ and elemental concentrations in metamorphic garnet from southeastern Vermont, USA. Geochim Cosmochim Acta 57:2585–2597

Zack T, Rivers T, Foley SF (2001) Cs-Rb-Ba systematics in phengite and amphibole: an assessment of fluid mobility at 2.0 GPa in eclogites from Trescolmen, Central Alps. Contrib Mineral Petrol 140:651–669